Tectonic and climatic impacts on environmental evolution in East Asia during the Palaeogene

Hanchao Jiang[1], Jinyu Zhang[1], Siqi Zhang[1], Ning Zhong[2], Shiming Wan[3], Ian Alsop[4], Hongyan Xu[1], Qiaoqiao Guo[1], and Zhen Yan[2]

[1]Institute of Geology, China Earthquake Administration
[2]Institute of Geology, Chinese Academy of Geological Sciences
[3]Institute of Oceanology, Chinese Academy of Sciences
[4]University of Aberdeen

November 24, 2022

Abstract

Palaeogene Environmental evolution in East Asia remains ambiguous. Here we present integrative work including magnetostratigraphy, grain-size, geochemistry, and clay minerals from a 1609-m-thick fluviolacustrine sequence in eastern China. The results reveal two periods of tectonic control alternating with three periods of climatic control of the sedimentary evolution. Tectonic activity, as revealed by particle coarsening and reduced weathering, occurs during 65.6-59 Ma around the study area, and increases in Asia during 55-54 Ma in response to the India-Eurasia collision. Weathering enhances gradually in East Asia during 59-55 Ma, probably caused by global warming. Continuous global warming during 54-50.5 Ma is responsible for enhanced aridification in East Asia. From 50.5 to 37.6 Ma, global cooling weakens evapotranspiration and increases westerlies-derived moisture. Both aspects increase effective moisture and chemical weathering in East Asia. These results shed light on how alternating tectonism and climate change impact environmental evolution in Asia during the Palaeogene.

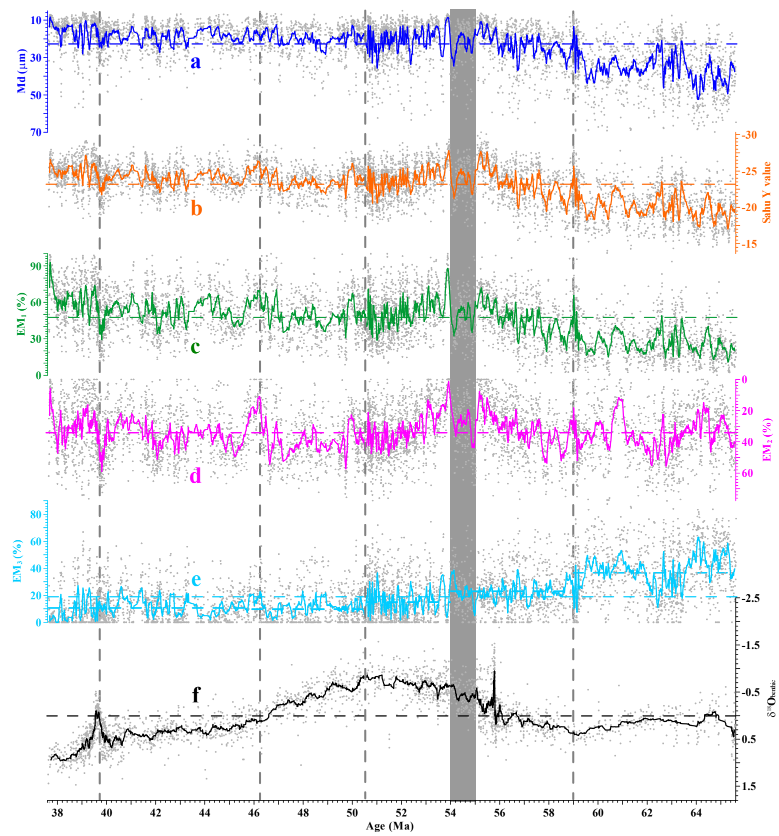

Md (μm)
a
Sahu Y value
b
EM1 (%)
c
EM2 (%)
d
EM3 (%)
e
f
δ18Obenthic
Age (Ma)

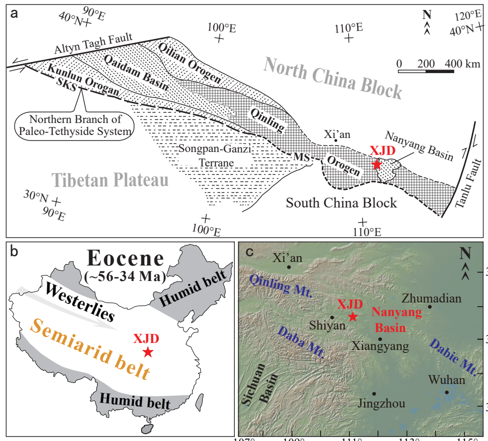
a
North China Block
Tibetan Plateau
South China Block
Altyn Tagh Fault
Qilian Orogen
Qaidam Basin
Kunlun Orogen
SKS
Northern Branch of Paleo-Tethyside System
Qinling
Orogen
Songpan-Ganzi Terrane
MS
Xi'an
XJD
Nanyang Basin
Tanlu Fault
0 200 400 km
b
Eocene
(~56-34 Ma)
Westerlies
Semiarid belt
Humid belt
Humid belt
XJD
c
Xi'an
Qinling Mt.
XJD
Nanyang Basin
Zhumadian
Shiyan
Daba Mt.
Xiangyang
Dabie Mt.
Sichuan Basin
Wuhan
Jingzhou

Fig. 1

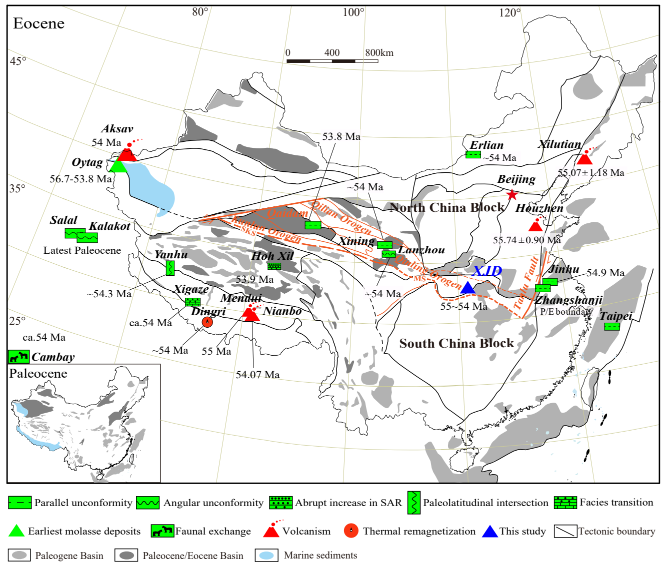
Eocene
80°
100°
120°
45°
35°
25°
0
400
800km
Aksav
54 Ma
Oytag
56.7-53.8 Ma
Salal
Kalakot
Latest Paleocene
Yanhu
~54.3 Ma
Xigaze
Dingri
Mendui
Nianbo
ca.54 Ma
~54 Ma
55 Ma
54.07 Ma
ca.54 Ma
Cambay
Hoh Xil
53.9 Ma
53.8 Ma
~54 Ma
Xining
Lanzhou
~54 Ma
Erlian
~54 Ma
Xilutian
55.07±1.18 Ma
Beijing
North China Block
Houzhen
55.74±0.90 Ma
XJD
55~54 Ma
Jinhu
54.9 Ma
Zhangshanji
P/E boundary
Taipei
South China Block
Qilian Orogen
Tan-Lu Fault
Paleocene
Parallel unconformity
Angular unconformity
Abrupt increase in SAR
Paleolatitudinal intersection
Facies transition
Earliest molasse deposits
Faunal exchange
Volcanism
Thermal remagnetization
This study
Tectonic boundary
Paleogene Basin
Paleocene/Eocene Basin
Marine sediments

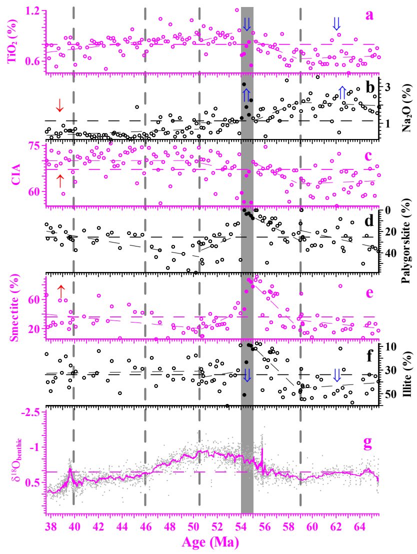

TiO2 (%)
Na2O (%)
CIA
Palygorskite (%)
Smectite (%)
Illite (%)
δ18Obenthic
a
b
c
d
e
f
g
Age (Ma)

Tectonic and climatic impacts on environmental evolution in East Asia during the Palaeogene

H. Jiang[a*], J. Zhang[a], S. Zhang[a, b], N. Zhong[a], S. Wan[c],

G. I. Alsop[d], H. Xu[a], Q. Guo[a, b], Z. Yan[e]

a. State Key Laboratory of Earthquake Dynamics, Institute of Geology, China Earthquake Administration, Beijing 100029, China.

b. College of Earth Sciences, University of Chinese Academy of Sciences, Beijing 100049, China.

c. Key Laboratory of Marine Geology and Environment, Institute of Oceanology, Chinese Academy of Sciences, Qingdao 266071, China

d. Department of Geology and Geophysics, School of Geosciences, University of Aberdeen, United Kingdom.

e. Institute of Geology, Chinese Academy of Geological Sciences, 26 Baiwanzhuang Rd, Beijing 100037, China.

[*]Corresponding author

E-mail: hcjiang@ies.ac.cn; hanchaojiang@hotmail.com (H. Jiang)

Key points

Tectonic activity occurred during 65.6-59 Ma in East Asia and strengthened during 55-54 Ma in response to the India-Eurasia collision.

In East Asia, global warming led to enhanced weathering during 59-55 Ma and aridification during 54-50.5 Ma.

Global cooling between 50.5-37.6 Ma increased westerlies-derived moisture and enhanced chemical weathering in East Asia.

Abstract

Palaeogene environmental evolution in East Asia remains ambiguous. Here we present integrative work including magnetostratigraphy, grain-size, geochemistry, and clay mineralalogy from a 1609-m-thick fluviolacustrine sequence in eastern China. The results reveal two periods of tectonic control alternating with three periods of climatic control on the sedimentary evolution. Tectonic activity in the study area, as revealed by particle coarsening and reduced weathering, occurred during 65.6-59 Ma and strengthened in Asia during 55-54 Ma in response to the India-Eurasia collision. Weathering gradually enhanced in East Asia during 59-55 Ma, probably caused by global warming. Continuous global warming during 54-50.5 Ma is responsible for enhanced aridification in East Asia. From 50.5 to 37.6 Ma, global cooling weakened evapotranspiration and increased westerlies-derived moisture. Both aspects increased effective moisture and chemical weathering in East Asia. These results shed light on how alternating

tectonism and climate change impacted environmental evolution in Asia during the Palaeogene.

Keywords: Fluviolacustrine sediments; Palaeogene; East Asia; Environmental evolution; Tectonism; Climate change

Plain language summary

Most investigations in sedimentary basins generally focus exclusively on climatic signals at the expense of tectonic inputs. In this work, we extract both climatic and tectonic signals from long fluviolacustrine sediment records in eastern China comprehensively and objectively. We find that environmental evolution during the Paleogene of East Asia was dominated by tectonism during 65.6-59 Ma and 55-54 Ma, and by climatic changes during 59-55 Ma and 54-37.6 Ma. This work not only constrains the India-Asia collision to a short 55-54 Ma interval for the first time, but also offers a sound explanation for one of the most important but disputed issues of eolian sediments in the North Pacific Ocean.

1. Introduction

It has previously been established that tectonic activity influences the evolution of fluviolacustrine sedimentary sequences by affecting the provenance supply, while climate change modifies the sedimentary record through weathering and denudation (Najman, 2006). During the Early Cenozoic, many rifted basins developed in eastern China, while an array of compressional basins formed in western China, mostly due to the India-Eurasia collision and continued convergence (Yin and Harrison, 2000) and/or subduction of the western Pacific Plate (Northrup et al., 1995). Most of these basins are filled with non-marine sediments (Ye et al., 1993) and the documented signals suggest that the environmental evolution has been driven mainly by tectonic activity and/or climate change (Ye et al., 1993).

The Qinling-Qilian-Kunlun orogenic system (QQKOS) extends for ~3000 km from east to west and formed in response to late Mid-Proterozoic to Cenozoic tectonism (Peltzer et al., 1985; Meng and Zhang, 2000). The QQKOS represents an important tectonic zone in Asia linking the India-Eurasia collision with extensive deformation in eastern China (Peltzer et al., 1985; Meng and Zhang, 2000) (Figure 1). Field observations show that the faults of the QQKOS are still active today and may have undergone several tens of kilometres of post-Eocene left-lateral displacement (Peltzer et al., 1985). However, the impact of the India-Eurasia collision on eastern China during the Palaeogene, which represents the critical period of the India-Eurasia collision, has not been determined. On the other hand, a broad belt of aridity stretched across China from west to east during the Palaeogene (Sun and Wang, 2005), overlapping spatially with the QQKOS, with only the southern-most and northeastern China being dominated by more humid conditions (Sun and Wang, 2005) (Figure 1b). Under this overall dry environment, voluminous windblown deposits developed widely in fault-bounded basins of varying scales around the QQKOS during the Palaeogene (Meng and Zhang, 2000; Jiang et al., 2014). Exploring such a long terrestrial sedimentary sequence as preserved in the Paleogene of East Asia can help elucidate the terrestrial responses to both greenhouse climate change and to tectonism like the India-Eurasia collision (Gao et al., 2021).

In this study, we present a 1609-m-thick Paleocene-Eocene fluviolacustrine sedimentary sequence at Xijiadian (XJD) town (32°46′N, 111°12′E) in the Nanyang Basin of the eastern QQKOS (Figure 1). This stratigraphic record enables us to distinguish the relative roles of tectonic drivers and climatic drivers in the environmental evolution of East Asia during the Palaeogene. It is of profound scientific significance for signature extraction of climate change and tectonism from the long lacustrine sequences around the globe during this geologic period.

2. Geographic and geological setting

The studied section lies in the western Nanyang Basin, situated in the eastern QQKOS between the North and the South China blocks (Figure 1). Faults, hydrology, and lithology in the study area are generally distributed along the WNW-ESE and NEN-SWS directions (Jiang et al., 2014). In the north, mainly Cambrian (limestone and shale) and middle Sinian (dolomitized limestone, silicic limestone, and sandstone interbedded with limestones) strata occur. The middle part of the study area is comprised of the Eocene Dacangfang Formation, which is dominated by reddish mudstone, silty mudstone, muddy siltstone, sandy conglomerate and conglomerate. In the south, the well-exposed Wudang quartz-sericite schist is interbedded with metasandstone and biotite-albite schist (Jiang et al., 2014).

Eastern China is currently influenced by the East Asian Summer Monsoon rainfall and is well vegetated. Therefore, long sedimentary sequences exposed in the eastern QQKOS (Figure 1) offer the rare chance to reconstruct the evolutionary history of a sedimentary environment driven by tectonic activity and climate change in East Asia.

3. Methods

Palaeomagnetic samples were drilled and oriented by compass. The average sampling interval was 0.8 m. Palaeomagnetic specimens were analyzed at the Paleomagnetism and Environmental Magnetism Laboratory in the Key Laboratory of Western China's Environmental System in Lanzhou University using the same demagnetizing and measuring procedures as Jiang et al. (2014).

In addition to the 4279 samples for the Eocene strata (Jiang et al., 2014), a total of 1598 samples were collected from the Paleocene sediments of the XJD section for grain-size analysis at a stratigraphic sampling interval of 0.09-1.28 m with a mean of 0.26 m. Organic material and carbonate were removed sequentially in grain size analysis. The samples were then analyzed using a Mastersizer 3000 laser grain-size analyzer at the State Key Laboratory of Earthquake Dynamics, Institute of Geology, China Earthquake Administration, Beijing, China.

Major and trace elemental concentrations were determined at the Analytical Laboratory of Beijing Research Institute of Uranium Geology using a Philips PW2404 X-ray Fluorescence Spectrometer and a Finnigan MAT HR-ICP-MS (Element I) instrument, respectively. Clay mineral and Sr-Nd isotope analysis were carried out on the < 2 μm fraction, which was separated using the Stokes' settling velocity principle, after the removal of carbonate and organic matter. Clay minerals were identified by

X-ray diffraction (XRD) using a D8 ADVANCE diffractometer with CuK (alpha) radiation (40 kV, 40 mA) in the Laboratory of the Institute of Oceanology, Chinese Academy of Sciences.

4. Results

4.1. Chronology of the XJD sequence

This new magnetostratigraphic work focuses on the 420-m-thick Paleocene sequence of the XJD section with 525 samples. Five normal (N_1-N_5) and five reversed (R_1-R_5) magnetic polarity zones are observed (Supp. Figures 2-4). Together with previous work on the Eocene strata and the constraints of a mammalian fossil *Rhombomylus cf. turpanensis* of the late Early Eocene at the Qingtangling site (~981 m at depth) (Jiang et al., 2014), the XJD magnetic polarity column unambiguously and reliably correlates with the Geomagnetic Polarity Timescale (Ogg, 2012) (Supp. Figure 5), suggesting that the XJD sequence is continuous and spans from 65.6 Ma to 37.6 Ma.

4.2. Provenance of the XJD fine-grained sediments

A total of 5877 grain-size samples are analyzed with a mean sampling interval of 0.27 m (equivalent to 4.76 ka). Systematic grain-size analysis shows that the median grain size (Md) varies between 5.0 µm and 69.9 µm, with a mean of 22.6 µm (Figure 2a). The Sahu Y value, determined by the mean grain size, standard deviation, skewness and kurtosis, is normally used to recognize an aeolian environment (Sahu, 1964) (Supplementary Note 1). The Y values of all samples range from -30.3 to -13.7, lower than the threshold value of -2.74 (Figure 2b), supporting their windblown origin (Jiang et al., 2014). Furthermore, major and trace element compositions are often used to trace the provenance of dust deposits (Ding et al., 2001; Jahn et al., 2001; Ferrat et al., 2011). The major and trace element abundances of 136 XJD fluviolacustrine fine samples, which are evenly distributed through the entire sequence, show an exponential linear relationship with those of the loess-soil units from the Chinese Loess Plateau (CLP) (Ding et al., 2001) (Supp. Figure 9), further corroborating their windblown origin.

The $^{143}Nd/^{144}Nd$ ratios of ten analyzed XJD samples display a restricted range of -11.6 ~ -9.7 (mean $\varepsilon_{Nd} \approx -10.65 \pm 0.95$) (Supplementary Note 2), indicating a relatively young and uniform upper crustal source for the XJD fine-grained sediments (Jahn et al., 2001). This is consistent with the typical upper crustal patterns revealed by $(La/Yb)_N$ (3.8-14.4, mean 10.4) and Eu/Eu* (0.56-0.76, mean 0.64) from the XJD sequence, which are typical of dust particles of loess-soil units from the CLP (Jahn et al., 2001).

4.3. Variations in the XJD grain-size record

Numerical unmixing of grain-size distribution data into constituent components, known as end-member analysis (EMA), can yield valuable information on geological processes (Weltje, 1997; Paterson and Heslop, 2015; Jiang et al., 2017). The multiple correlation coefficient (R^2) and angle deviation are commonly used to determine goodness-of-fit (Paterson and Heslop, 2015), and one important principle is to explain the observed compositional variation with a minimum number of end members (Weltje, 1997). The grain size of all 5877 samples is mainly concentrated in the range of 0-100 μm with a unimodal distribution (Supp. Figure 8a). To approximate the observed compositional variation, one to five end members are modeled by EMA in this study. The correlation maps for R^2 and angle deviation with number of end members suggest that end-member modeling improves greatly from two to three end members, but improves less from three to four end members (Supp. Figure 8b & c). Accordingly, three end-members are the minimum number that are the closest to the truth (Supp. Figure 7), and they include EM_1 (0.3-243.0 μm, peak at 6.9 μm), EM_2 (0.5-306.6 μm, peak at 29.5 μm), and EM_3 (0.7-546.6 μm, peak at 78.1 μm) (Supp. Figure 8). EM_1 (0-100%, mean 47.2%) can be transported through long-term suspension, whereas EM_2 (0-77.8%, mean 34.1%) and EM_3 (0-90.6%, mean 18.7%) (Figure 2c-e) represent regional and local windblown sediments, respectively (Pye, 1987; Jiang et al., 2014).

We averaged three end-members with a window width of 21 points to detect their varying trends. There are two patterns: dramatic changes and steady evolution. The grain-size record from 65.6 to 59 Ma has the strongest fluctuations with the largest amplitude (7.2-69.9 μm) and the maximum Md of the sequence (mean 34.8 μm). The local windblown fraction (EM_3) reaches 90.6%, with the highest mean of 36.8% during 65.6-59 Ma. The dust particles become coarse at 55-54 Ma, with an abrupt increase in EM_2 and a corresponding decrease in EM_1, similar to a 1-Myr-duration wedge (Figure 2 c & d). In contrast, the other periods display a relatively steady evolution; specifically, the dust particles gradually fine from 59 Ma to 55 Ma, coarsen from 54 Ma to 50.5 Ma and slowly fine again from 50.5 Ma to 37.6 Ma (Figure 2).

4.4. Major and trace element variations

The addition of fresh material to sedimentary basins commonly results in a decrease in the immobile element content and an increase in the mobile element content, whereas stepwise weathering and leaching usually induce the opposite change.

During 65.6-59 Ma, the content of immobile TiO_2 (0.5-0.9%) has the lowest mean (0.6%) of the sequence with unstable oscillations (Figure 3a). It steadily increases from 59 to 55 Ma, decreases significantly during 55-54 Ma, and decreases from 54 to 37.6 Ma but remains above the overall average. The abundance of mobile Na_2O (0.5-3.52%) and the molar ratios of Na_2O/Al_2O_3 (0.03-0.49) during 65.6-55 Ma are the most scattered but their average values (2.05% and 0.24) are the highest of the whole sequence, which then exhibits a decreasing trend from 59 to 55 Ma (Figure 3b). They increase significantly during 55-54 Ma and oscillate generally below the average values after 54 Ma. The other major elements and 17 trace elements all have distinct changes at 55-54 Ma (Supp. Figures 10-11, Supplementary Note 4). Noticeably, the ratios of Y/ΣREE, Y/Nd_{PAAS}, $(Eu/Eu^*)_{PAAS}$, and $(La/Er)_{PAAS}$ normalized to post-Archean Australian shale (PAAS) and are utilized to identify provenance changes independent of particle size (Ferrat et al., 2011). At 55-54 Ma, the first three ratios increase dramatically (Supp. Figure 12a-c), whereas the last ratio decreases significantly (Supp. Figure 12d). They are followed by the opposite trends for these four ratios after ~54 Ma.

The chemical index of alteration (CIA) is generally used as an indicator of the degree of weathering of sediments (Supplementary Note 5). The CIA values (55.3-75.7) of the analyzed samples have an overall low average of 67.2 (Figure 3c), indicating deposition under a dry and weak-weathering environment. During 65.6-59 Ma, the CIA values fluctuate strongly between 55.3 and 72.3, with a mean value of 63.0. The CIA values increase from 59 to 55 Ma (mean 66.1) and decrease abruptly at 55-54 Ma with the lowest average value of 60.8 for the whole sequence. After 54 Ma, the CIA values show small oscillations, with most samples above the average (67.2) (Figure 3c).

4.5. Clay minerals and their Sr-Nd isotopic variations

The clay mineral assemblages of the XJD sequence are dominated by smectite (6-91%, mean 36%), illite (7-60%, mean 34%) and palygorskite (0-59%, mean 25%), with minor amounts of chlorite (0-9%, mean 2%) and kaolinite (0-7%, mean 2%) (Figure 3d-f, Supp. Figure 14, Supp. Table 2). During 65.6-59 Ma, the content of illite (12-58%, mean 43%) and the ratio of illite/smectite (0.15-6.50, mean 2.24) are not only the highest but also the most scattered of the sequence, while most smectite values are lower than the average (Figure 3e & f). Palygorskite shows extremely scattered values (Figure 3d). From 59 Ma to 55 Ma, content variation of these major clay minerals become stable, with decrease in illite and palygorskite and increase in smectite (Figure 3d-f). At 55-54 Ma, illite and the illite/smectite ratio increase rapidly, smectite decreases significantly, and palygorskite remains the lowest of the sequence. From 54 Ma to 50.5 Ma, smectite decreases and palygorskite and the illite/smectite ratio increase, while these three proxies show the opposite trend from 50.5 Ma to 37.6 Ma.

A strong inverse relationship between smectite and palygorskite reveals the authigenic transformation of palygorskite from smectite (Figure 3d & e, Supp. Figure 16a). Furthermore, a stronger inverse relationship between illite and the sum of palygorskite and smectite (Supp. Figure 16b) suggests that the illite in the study area has been transformed into palygorskite and smectite. Clay components of the XJD fluviolacustrine sediments have Sr-Nd isotopic features similar to those from the northern margin of the TP instead of those from the eastern QQKOS (Supplementary Note 2). This implies that they are mainly transported by wind from the northern margin of the TP.

5. Discussion and implications

Some layers of sandstone and sandy conglomerate are occasionally developed in the XJD section, reflecting the fluvial contribution in the Nanyang Basin (Jiang et al., 2014). This basin is located in the piedmont area of the East Qinling Mountains (Figure 1c). The floodplains may provide silt particles for the Nanyang Basin similar to those from the western Qinling Mountains for the Tianshui Basin (Liu et al., 2019). However, there is no evidence in the field of hydrodynamic waxing or waning expressed as upward coarsening or fining particles. Correspondingly, sedimentary structures such as cross-bedding and ripples related to current action were rarely observed in the XJD section. Instead, massive structure, a typical feature of dust deposition (Ding et al., 2001), commonly exists in the XJD section. Noticeably, fluvial sedimentation generally has a momentary process with a high-energy environment while dust deposition occurs over a long duration with the inherent characteristics of a low-energy environment. Accordingly, we focus on slow deposition of fine dust particles rather than fluvial deposits in this study.

5.1. Weathering affected by climate change

From 59 to 55 Ma, the XJD dust particles consistently become finer (Figure 2). The immobile TiO_2 content, CIA, and smectite increase, while the mobile Na_2O content, the Na_2O/Al_2O_3 ratio, the illite/smectite ratio and palygorskite proportion decrease (Figure 3). These trends are probably due to enhanced chemical weathering induced by global warming, as revealed by the benthic $\delta^{18}O$ record (Cramer et al., 2009) (Figure 2f).

From 54 Ma to 50.5 Ma, the local particle supply EM_3 decreases below the average, implying a tectonically stable environment (Figure 2e). However, the XJD dust particles become coarse (Figure 2a) as the regional particle supply EM_2 increases above the average (Figure 2d). In addition, illite content and CIA increase slightly, while the illite/smectite ratio and palygorskite (probably transformed from smectite) increase significantly (Figure 3). These results indicate a slight weathering-enhanced and high-alkalinity (Singer, 1980) sedimentary environment in the Nanyang Basin. This enhanced aridification (Jiang et al., 2014) is likely to result from sustained warming globally based on the benthic $\delta^{18}O$ record (Cramer et al., 2009) (Figure 2f).

The period from 50.5 to 37.6 Ma is characterized by slow fining of the XJD dust particles, with the smallest mean Md (18.2 μm) and the lowest mean EM_3 proportion (10.6%) of the sequence. The generally high CIA values and TiO_2 contents and low contents of Na_2O and ratio of Na_2O/Al_2O_3 suggest a slightly increased weathering, though with a generally low intensity under an arid environment (Figure 3a-c). The stepwise content decrease in palygorskite from 50.5 Ma to 37.6 Ma indicates a decreased alkalinity and thus an increased humidity of the depositional environment (Figure 3d). The increase in smectite and the decrease in the illite/smectite ratio imply increased weathering in the study area, although illite remains relatively stable in content (Figure 3e & f). Here we propose that global cooling from 50.5 Ma to 37.6 Ma weakened evapotranspiration, enhanced the westerly circulation (Jiang et al., 2014) and consequently increased moisture carried by the westerly wind (Gao et al., 2021). Both aspects increased effective moisture and consequently enhanced chemical weathering in East Asia. This interpretation is also supported by the positive response of the XJD sedimentation to two salient climatic events. The appearance of ice in the Arctic at ~46 Ma (Moran et al., 2006) indicates significant global cooling. The obvious response of the XJD sequence at ~46 Ma includes the fining of dust particles (Figure 2), high CIA values and smectite contents (Figure 3c & e), low Na_2O/Al_2O_3 and illite/smectite ratios and reduced alkalinity as revealed by the decrease in palygorskite content (Figure 3b, d & f). A global warming event at ~40 Ma related to a brief reversal of the long-term Eocene cooling trend (Bohaty and Zachos, 2003; Bohaty et al., 2009), induced the opposite responses to those at ~46 Ma (Figures 2 and 3b-e). Hence, during the Palaeogene, East Asia was controlled by a planetary climate rather than a monsoon climate.

5.2. Enhanced tectonic activity at 55-54 Ma

The period of 65.6-59 Ma is characterized by the highest mean values and the strongest oscillations in the local dust supply (EM_3), the lowest average TiO_2 content, the highest average Na_2O/Al_2O_3 and illite/smectite ratios, and a low mean CIA (63.0) in the XJD sequence. Additionally, the period 55-54 Ma features pronounced increases in the regional dust supply (EM_2) and the Na_2O/Al_2O_3 and illite/smectite ratios, and significant decreases in the immobile TiO_2 content, CIA, and smectite. These features indicate the significant addition of fresh material into the XJD sediments and a resultant decrease in weathering. We ascribe these changes to tectonic activity around the eastern QQKOS during 65.6-59 Ma, and significantly strengthened tectonic activity in Asia during 55-54 Ma in response to the India-Eurasia collision at ~55 Ma as revealed by the Indian Ocean magnetic anomalies (Powell and Conaghan, 1975). In addition to the effects observed in our study area, the intense tectonic activity during 55-54 Ma produces a widespread disconformity (Zheng et al., 1999; Singh, 2003; Wang et al., 2010; Xue et al., 2013; Zhang et al., 2014; Zhou et al., 2019; Fang et al., 2019), the onset of India-Eurasia terrestrial faunal exchange (Clementz et al., 2011), an abrupt increase in sediment accumulation (Jin et al., 2018), facies transitions (Orme et al., 2015), palaeolatitudinal intersection (Ma et al., 2014), thermal remagnetization (Tong et al., 2008), the formation of many basins in Asia (Sun and Jiang, 2013), and the closure of the Neo-Tethys Ocean (Li et al., 2015) (Figure 4, Supplementary Note 6 and Supplementary Table 3). Furthermore, the intense tectonic activity during 55-54 Ma also generates widespread magmatic eruptions in Asia (Li et al., 1989; Bazhenov and Mikolaichuk, 2002; Zhou et al., 2004; Sun et al., 2010; Chen et al., 2014). These features for the first time collectively constrain the India-Eurasia collision to a short interval from 55-54 Ma, which is consistent with the timing of an almost complete halt to the northward motion of India (Sclater and Fisher, 1974), the end of suturing and the beginning of the so-called hard collision at ~55 Ma (Klootwijk et al., 1992).

5.3. Impact on the North Pacific Ocean

The eolian sediments in the North Pacific Ocean display sharp decreases in grain size from continuously coarse grained in the Paleocene to continuously fine grained in the Eocene, while the peak accumulation rate decreases by almost a factor of 3 across the Paleocene/Eocene (P/E) boundary (Janecek and Rea, 1983; Rea, 1994). Both phenomena have for decades remained enigmatic due to the absence of systematic investigations into long continental sedimentary records. Based on our work, we propose that the occurrence of tectonic activity around the QQKOS during 65.6-59 Ma and its enhancement in Asia at 55-54 Ma in response to the India-Eurasia collision, are responsible for both phenomena. Strong earthquakes associated with tectonic activity can generate large amounts of dust particles in arid to semiarid regions (Jiang et al., 2017), which could have been transported to the basins around the QQKOS and even as far as the North Pacific Ocean during the Paleogene. In the Nanyang Basin, the dust particles are generally coarse during 65.6-55 Ma and remain mostly fine after 54 Ma (Figure 2), which contributes to our understanding of the patterns of aeolian sediments in the North Pacific Ocean (Janecek and Rea, 1983; Rea, 1994). This is the first study to develop a new source-to-sink model that links basin deposition during the Paleogene in Asia to pelagic sedimentation in the North Pacific Ocean in response to the India-Eurasia collision. Noticeably, the availability of dust particles in Asia, instead of transport capacity, plays the primary role in deposition of the aeolian sediments in the North Pacific Ocean from the Paleocene to the Eocene, given that the low thermal gradients and less vigorous atmospheric circulation during this period (Janecek and Rea, 1983; Suan et al., 2017) could have weakened the dynamics of dust transport.

Acknowledgements

This work is financially supported by the National Natural Science Foundation of China (41572346) and National Nonprofit Fundamental Research Grant of China, Institute of Geology, China Earthquake Administration (IGCEA1906). We feel grateful to Prof. Jin Meng, Prof. Peter D. Clift and Dr. Jessica A. Thompson Jobe for the valuable comments and constructive suggestions. We thank Dr. Zuolin Chen and Ms Xue Mao for assistance in the field, and Ms Yanhao Li and Mr Youliang Bai for help in the laboratory. We appreciate Prof. Lucy Flesch (editor) for handling our manuscript and two anonymous reviewers for constructive reviews. Source data are provided with this paper and are deposited in Mendeley (doi: 10.17632/gdppp4r97d.1).

Reference

Bazhenov, M. L., & Mikolaichuk, A. V. (2002). Paleomagnetism of Paleogene basalts from the Tien Shan, Kyrgyzstan: rigid Eurasia and dipole geomagnetic field. Earth and Planetary Science Letters, 195(1–2), 155–166. https://doi.org/10.1016/S0012-821X(01)00586-6

Bohaty, S. M., & Zachos, J. C. (2003). Significant Southern Ocean warming event in the late middle Eocene. Geology, 31(11), 1017–1020. https://doi.org/10.1130/G19800.1

Bohaty, S. M., Zachos, J. C., Florindo, & Delaney, M. L. (2009). Coupled greenhouse warming and deep-sea acidification in the middle Eocene. Paleoceanography, 24. https://doi.org/10.1029/2008PA001676

Chen, Z., Ding, Z., Tang, Z., Wang, X., & Yang, S. (2014). Early Eocene carbon isotope excursions: Evidence from the terrestrial coal seam in the Fushun Basin, Northeast China. Geophysical Research Letters, 41, 3559-3564. https://doi.org/10.1002/2014GL059808

Clementz, M., Bajpai, S., Ravikant, V., Thewissen, J. G. M., Saravanan, N., Singh, I. B., & Prasad, V. (2011). Early Eocene warming events and the timing of terrestrial faunal exchange between India and Asia. Geology, 39(1), 15–18. https://doi.org/10.1130/G31585.1

Cramer, B. S., Toggweiler, J. R., Wright, J. D., Katz, M. E. & Miller, K. G. (2009) Ocean overturning since the Late Cretaceous: Inferences from a new benthic foraminiferal isotope compilation. Paleoceanography, 24(4). PA4216, 1-14. https://doi.org/10.1029/2008pa001683

Ding, Z., Sun, J., Yang, S. & Liu, T. (2001). Geochemistry of the Pliocene red clay formation in the Chinese Loess Plateau and implications for its origin, source provenance and paleoclimate change. Geochimica et Cosmochimica Acta, 65(6), 901–913. https://doi.org/10.1016/S0016-7037(00)00571-8

Fang, X., Fang, Y., Zan, J., Zhang, W., Song, C., Appel, E., et al. (2019). Cenozoic magnetostratigraphy of the Xining Basin, NE Tibetan Plateau, and its constraints on paleontological, sedimentological and tectonomorphological evolution. Earth-Science Reviews, 190, 460–485. https://doi.org/10.1016/j.earscirev.2019.01.021

Ferrat, M., Weiss, D. J., Strekopytov, S., Dong, S., Chen, H., Najorka, J., et al. (2011). Improved provenance tracing of Asian dust sources using rare earth elements and selected trace elements for palaeomonsoon studies on the eastern Tibetan Plateau. Geochimica et Cosmochimica Acta, 75(21), 6374–6399. https://doi.org/10.1016/j.gca.2011.08.025

Gao, Y., Ibarra, D. E., Caves Rugenstein, J. K., Chen, J., Kukla, T., Methner, K., et al. (2021). Terrestrial climate in mid-latitude East Asia from the latest Cretaceous to the earliest Paleogene: A multiproxy record from the Songliao Basin in northeastern China. Earth-Science Reviews, 216, 103572. https://doi.org/10.1016/j.earscirev.2021.103572

Jahn, B. M., Gallet, S., & Han, J. (2001). Geochemistry of the Xining, Xifeng and Jixian sections, Loess Plateau of China: eolian dust provenance and paleosol evolution during the last 140 ka. Chemical Geology, 178, 71-94. https://doi.org/10.1016/S0009-2541(00)00430-7

Janecek, T. R., & Rea, D. K. (1983). Eolian deposition in the northeast Pacific Ocean: Cenozoic history of atmospheric circulation. Geological Society of America Bulletin, 94(6), 730–738.

https://doi.org/10.1130/0016-7606(1983)94<730:EDITNP>2.0.CO;2

Jiang, H., Zhong, N., Li, Y., Ma, X., Xu, H., Shi, W., et al. (2017). A continuous 13.3-ka record of seismogenic dust events in lacustrine sediments in the eastern Tibetan Plateau. Scientific Reports, 7(1), 15686. https://doi.org/10.1038/s41598-017-16027-8

Jiang, H., Zhong, N., Li, Y., Xu, H., Ma, X., Meng, Y., & Mao, X. (2014). Magnetostratigraphy and grain size record of the Xijiadian fluviolacustrine sediments in East China and its implied stepwise enhancement of the westerly circulation during the Eocene period. Journal of Geophysical Research: Solid Earth, 119(10), 7442–7457. https://doi.org/10.1002/2014JB011225

Jin, C., Liu, Q., Liang, W., Roberts, A. P., Sun, J., Hu, P., et al. (2018). Magnetostratigraphy of the Fenghuoshan Group in the Hoh Xil Basin and its tectonic implications for India–Eurasia collision and Tibetan Plateau deformation. Earth and Planetary Science Letters, 486, 41–53. https://doi.org/10.1016/j.epsl.2018.01.010

Klootwijk, C. T., Gee, J. S., Peirce, J. W., Smith, G. M., & Mcfadden, P. L. (1992). An early India-Asia contact: Paleomagnetic constraints from Ninetyeast Ridge, ODP Leg 121. Geology, 20(5), 395-398. https://doi.org/10.1130/0091-7613(1992)020<0395:AEIACP>2.3.CO;2

Li, J., Hu, X., Garzanti, E., An, W., & Wang, J. (2015). Paleogene carbonate microfacies and sandstone provenance (Gamba area, South Tibet): Stratigraphic response to initial India–Asia continental collision. Journal of Asian Earth Sciences, 104(may 15), 39–54. https://doi.org/10.1016/j.jseaes.2014.10.027

Li, J.R., Xu, J.L., Yao, Y.M. & Xiang, W.D., 1989. Paleocene Houzhen formation in Changwei, Shandong Province. Chin. Sci. Bull. 34, 1882–1884.

Liu, S., Li, J., Stockli, D. F., Song, C., Guo, B., Stockli, L. D., et al. (2019). Reappraisal of Miocene eolian deposition in Tianshui Basin, China, based on an investigation of stratigraphy and provenance. Geological Society of America Bulletin, 131(7–8), 1312–1332. https://doi.org/10.1130/B32056.1

Ma, Y., Yang, T., Yang, Z., Zhang, S., Wu, H., Li, H., et al. (2014). Paleomagnetism and U-Pb zircon geochronology of Lower Cretaceous lava flows from the western Lhasa terrane: New constraints on the India-Asia collision process and intracontinental deformation within Asia. Journal of Geophysical Research. Solid Earth: JGR, 119(10), 7404–7424. https://doi.org/10.1002/2014JB011362

Meng, Q., & Zhang, G. (2000). Geologic framework and tectonic evolution of the Qinling orogen, central China. Tectonophysics, 323(3–4), 183–196. https://doi.org/10.1016/S0040-1951(00)00106-2

Moran, K., Backman, J., Brinkhuis, H., Clements, S. C., Cronin, T., Dickens, G. R., et al. (2006). The Cenozoic palaeoenvironment of the Arctic Ocean. Nature, 441, 601–605. https://doi.org/10.1038/nature04800

Najman, Y. (2006). The detrital record of orogenesis: A review of approaches and techniques used in the Himalayan sedimentary basins. Earth-Science Reviews, 74(1–2), 1–72. https://doi.org/10.1016/j.earscirev.2005.04.004

Northrup, C. J., Royden, L. H., & Burchfiel, B. C. (1995). Motion of the Pacific plate relative to Eurasia and its potential relation to Cenozoic extension along the eastern margin of Eurasia. Geology, 23(8), 719–722. https://doi.org/10.1130/0091-7613(1995)023<0719:MOTPPR>2.3.CO;2

Ogg, J. G. in *The Geologic Time Scale* (eds Gradstein, F. M., Ogg, J. G., Schmitz, M. D., & Ogg, G. M.) 85–113 (Elsevier, 2012).

Orme, D. A., Carrapa, B., & Kapp, P. (2015). Sedimentology, provenance and geochronology of the upper Cretaceous–lower Eocene western Xigaze forearc basin, southern Tibet. Basin Research, 27(4), 387–411. https://doi.org/10.1111/bre.12080

Paterson, G. A., & Heslop, D. (2015). New methods for unmixing sediment grain size data. Geochemistry, Geophysics, Geosystems, 16(12), 4494–4506. https://doi.org/10.1002/2015GC006070

Peltzer, G., Tapponnier, P., Zhitao, Z., & Qin, X. Z. (1985). Neogene and Quaternary faulting in and along the Qinling Shan. Nature, 317(6037), 500–505. https://doi.org/10.1038/317500a0

Powell, C.M. & Conaghan, P.J., 1975. Tectonic models of the Tibetan plateau. Geology 3, 727–731.

Pye, K. *Eolian dust and dust deposits* (Academic Press, 1987).

Rea, D. K. (1994). The paleoclimatic record provided by eolian deposition in the deep-sea: The geologic history of wind. Reviews of Geophysics, 35, 159-195. https://doi.org/10.1029/93rg03257

Sahu, B. K. (1964). Depositional mechanisms from the size analysis of clastic sediments. Journal of . Sedimentary. Petrology. 34(1), 73–83. https://doi.org/10.1306/74D70FCE-2B21-11D7-8648000102C1865D

Sclater, J. G. & Fisher, R. L. (1974). Evolution of the East: Central Indian Ocean, with emphasis on the tectonic setting of the Ninetyeast Ridge. Geological Society of America Bulletin, 85, 683–702. https://doi.org/10.1130/0016-7606(1974)85%3C683:eoteci%3E2.0.co;2

Singer, A. (1980). The paleoclimatic interpretation of clay minerals in soils and weathering profiles. Earth- Science Reviews, 15(4), 303–326. https://doi.org/10.1016/0012-8252(80)90113-0

Singh, B. P. (2003). Evidence of growth fault and forebulge in the Late Paleocene (57.9–54.7 Ma), western Himalayan foreland basin, India. Earth and Planetary Science Letters, 216(4), 717–724. https://doi.org/10.1016/S0012-821X(03)00540-5

Suan, G., Popescu, S. M., Suc, J. P., Schnyder, J., Fauquette, S., Baudin, F., et al. (2017). Subtropical climate conditions and mangrove growth in Arctic Siberia during the early Eocene. Geology, 45(6), 539–542. https://doi.org/10.1130/G38547.1

Sun, J., & Jiang, M. (2013). Eocene seawater retreat from the southwest Tarim Basin and implications for early Cenozoic tectonic evolution in the Pamir Plateau. Tectonophysics, 588, 27–38. https://doi.org/10.1016/j.tecto.2012.11.031

Sun, X., & Wang, P. (2005). How old is the Asian monsoon system? Paleobotanical records from China. Palaeogeography Palaeoclimatology Palaeoecology, 222(3–4), 181–222. https://doi.org/10.1016/j.palaeo.2005.03.005

Sun, Z., Jiang, W., Li, H., Pei, J., & Zhu, Z. (2010). New paleomagnetic results of Paleocene volcanic rocks from the Lhasa block: Tectonic implications for the collision of India and Asia. Tectonophysics, 490, 257-266. https://doi.org/10.1016/j.tecto.2010.05.011

Tong, Y., Yang, Z., Zheng, L., Yang, T., Shi, L., Sun, Z., & Pei, J. (2008). Early Paleocene Paleomagnetic Results from Southern Tibet, and Tectonic Implications. International Geology Review, 50(6), 546–562. https://doi.org/10.2747/0020-6814.50.6.546

Wang, Y., Meng, J., Beard, C., Li, Q., Ni, X., Gebo, D. L., et al. (2010). Early Paleogene stratigraphic sequences, mammalian evolution and its response to environmental changes in Erlian Basin, Inner Mongolia, China. Science China Earth Sciences, 53(12), 1918–1926. https://doi.org/10.1007/s11430-010-4095-8

Weltje, G. J. (1997). End-member modeling of compositional data: Numerical-statistical algorithms for solving the explicit mixing problem. Mathematical Geology, 29(4), 503–549. https://doi.org/10.1007/BF02775085

Xue, K., Ji, J., Zhang, K., Kou, X., Song, B., & Wang, C. (2013). Magnetostratigraphy and anisotropy of magnetic susceptibility of the Lulehe formation in the Northeastern Qaidam Basin. Acta Geologica Sinica - English Edition, 87(2), 576–587. https://doi.org/10.1111/1755-6724.12069

Ye, D.Q., et al., in *Tertiary in Petroliferous Regions of China*, 1-407 (Petroleum Industry Press, 1993).

Yin, A., & Harrison, T. M. (2000). Geologic Evolution of the Himalayan-Tibetan Orogen. Annual Review of Earth and Planetary Sciences, 28(1), 211–280. https://doi.org/10.1146/annurev.earth.28.1.211

Zhang, Y., Sun, D., Li, Z., Wang, F., Wang, X., Li, B., et al. (2014). Cenozoic record of aeolian sediment accumulation and aridification from Lanzhou, China, driven by Tibetan Plateau uplift and global climate. Global and Planetary Change, 120, 1–15. https://doi.org/10.1016/j.gloplacha.2014.05.009

Zheng, J. J., et al. *China Stratigraphic Code. Tertiary* (Geologic Press, 1999).

Zhou, S., Mo, X., Dong, G., Zhao, Z., Qiu, R., Guo, T., & Wang, L. (2004). ^{40}Ar-^{39}Ar geochronology of Cenozoic Linzizong volcanic rocks from Linzhou Basin, Tibet, China, and their geological implications. Chinese Science Bulletin, 49(18), 1970-1979. https://doi.org/10.1360/03wd0511

Zhou, X., Jiang, Z., Quaye, J., Duan, Y., Hu, C., Liu, C., & Han, C. (2019). Ichnology and sedimentology of the trace fossil-bearing fluvial red beds from the lowermost member of the Paleocene Funing Formation in the Jinhu Depression, Subei Basin, East China. Marine and Petroleum Geology, 99, 393–415. https://doi.org/10.1016/j.marpetgeo.2018.10.032

Figure captions

Figure 1. a. Diagram showing the genetic linkage between the Qinling and adjacent orogens to the west (Meng and Zhang, 2000). b. Distribution of semiarid belt and location of the Nanyang Basin (Sun and Wang, 2005). c. Topography around the Nanyang Basin (http://www.geomapapp.org/). Note that the Mianlue suture (MS) is connected to the Southern Kunlun suture (SKS), and the South Qinling and Kunlun orogens together represent a northern branch of the Palaeo-Tethyan orogenic system (Meng and Zhang, 2000). XJD refers to the Xijiadian section. Red star marks the location of the study area.

Figure 2. The median grain-size (Md) (a), Sahu Y value (b), and three grain-size end-member abundances (c-e) of the Xijiadian sequence in Hubei Province (eastern China) spanning 65.6-37.6 Ma plotted against palaeomagnetic ages and their correlation with the benthic $\delta^{18}O$ record (f) (Cramer et al., 2009). The Sahu Y value less than -2.74 indicates an aeolian environment (Sahu, 1964) (Supplementary Note 1). The gray dots define sample or data points. The solid lines represent a moving average with a window width of 21 points to detect their trends. The horizontal dashed lines indicate the average values of the records. The vertical dashed lines indicate the important shifts discussed in the text.

Figure 3. Comparison of varying values of TiO_2 (a), Na_2O/Al_2O_3 (b, molar ratio), CIA (c), palygorskite (d), smectite (e), and illite/smectite (f) in fluviolacustrine sediments from the Xijiadian sequence in Hubei Province (eastern China) with variations in the benthic $\delta^{18}O$ record (g) (Cramer et al., 2009). The grey points and open circles represent sample or data points. The dashed horizontal or oblique lines indicate the average or fitting trends. The vertical dashed lines and the gray band indicate the time points and intervals discussed in the text. The red single-line arrows indicate the variation of weathering while the blue double-line arrows indicate the variation in fresh material sources with upward arrows showing the trend of increase and vice versa.

Figure 4. Diagram showing the consistent kinematic properties of the Qinling-Qilian-Kunlun orogenic system (QQKOS) and locations with corroborating evidence of the strong tectonic activities at 55-54 Ma in Asia. These include stratigraphic unconformities, abrupt increases in the sediment accumulation rate (SAR), palaeolatitudinal intersection, facies transitions, molasse deposits, faunal exchange, volcanism, and thermal remagnetization (Supp. Table 3).

Tectonic and climatic impacts on environmental evolution in East Asia during the Paleogene

(Supplementary information)

1. Brief description of the Qinling Mountains

The Middle Paleozoic collision along the Shangdan suture led to the accretion of the South Qinling to the North Qinling while the Late Triassic collision resulted in widespread granitoid intrusions throughout the Qinling Mountains. The ultra-high-pressure (UHP) metamorphic rocks in the Tongbai-Dabie terrane should be related to the collision of the South Qinling and the South China block because the ages of UHP metamorphic rocks apparently cluster around the Late Triassic (Hacker et al., 1996). Thus, a two-stage collision, Middle Paleozoic and Late Triassic, resulted in the Qinling orogeny and led to final amalgamation of the North and South China blocks (Meng and Zhang, 2000).

Analysis of the present-day tectonic deformation of continental China, based on the global positioning system (GPS) measurements, indicates that the Tibetan Plateau (TP) deforms continuously from the southern margin of TP to eastern China (Zhang and Gan, 2008; Wang and Shen, 2020). This corroborates the previous recognition that slip rates for active faults are highest in the Himalayan collision zone and gradually decrease away from the collision zone into the adjacent active tectonic provinces (Xu and Deng, 1996). Intriguingly, the average strain rates of the South China and Ordos blocks are 2.9×10^{-9} and 5.8×10^{-9}, respectively, whereas the average strain rate across the block boundary is

2.7 × 10⁻⁸. This is an order of magnitude greater than those of the South China and North China (Supp. Figure 1), suggesting the rigid block property of the two blocks (Zhang and Gan, 2008) and the coherent kinematic properties of the Qilian-Qinling-Kunlun Orogenic System (QQKOS) (Figure 1).

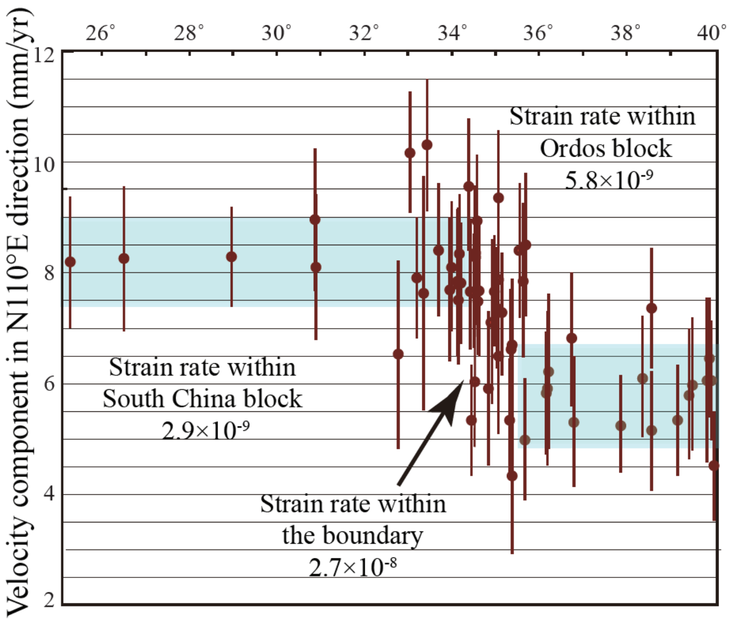

Supp. Figure 1. Relative motion between the South China and the Ordos blocks measured by global positioning system (GPS). The strain rate across the boundary between these two rigid blocks is an order of magnitude greater than that across the blocks (Zhang and Gan, 2008).

2. Paleomagnetic analysis

Progressive thermal demagnetization revealed one or two magnetic components following removal of a soft viscous overprint by temperature step 150 °C. Hematite is the major characteristic remanent magnetization (ChRM)-bearing minerals for most of the samples (Supp. Figure 2).

By principal component analysis, 230 out of the total of 525 samples were discarded due to unstable ChRM directions, the maximum angular deviation (MAD) larger than 15°, or excursional geomagnetic directions. Finally, ChRM directions isolated from 295 samples are interpreted as having been acquired during times of stable polarity.

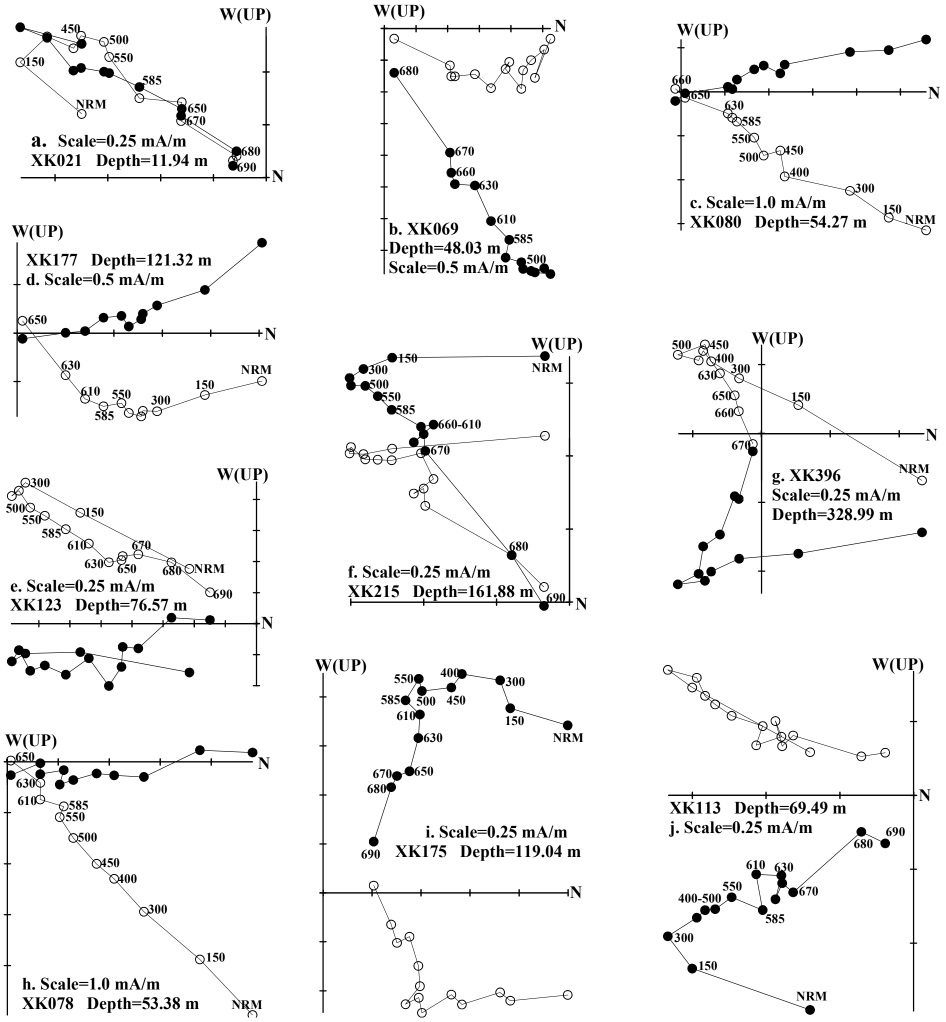

Supp. Figure 2. Orthogonal vector plots of representative specimens from the study section. Demagnetization steps in °C in all plots; solid (open) circles refer to the projection on the horizontal (vertical) plane in geographic coordinates; depth ranges from 0 to 420 m.

As for 295 samples, the overall site-mean direction is D_g = 6.6°, I_g = 54.3°, κ_g = 11.8, α_{95} = 2.4° before and D_s = 4.4°, I_s = 35.2°, κ_s = 12.3, α_{95} = 2.3° after tilt correction

(Supp. Figure 3a). A reversal test (McFadden and McElhinny, 1990) is positive with A classification (angle distance between site-mean directions of normal and reversed polarities is 3.2°, which is less than the critical angle of 4.9°). These ChRM directions of 295 samples were then grouped stratigraphically into 20 sites. For these 20 interval-mean directions, the reversal test (McFadden and McElhinny, 1990) was positive with B classification (angle distance between interval-mean directions of normal and reversed polarities is 2.2°, which is less than the critical angle of 7.8°). The overall group-mean direction is $D_g = 6.1°$, $I_g = 55.7°$, $\kappa_g = 50.2$, $\alpha_{95} = 4.4°$ before and $D_s = 3.8°$, $I_s = 34.9°$, $\kappa_s = 74.6$, $\alpha_{95} = 3.6°$ after tilt correction (Supp. Figure 3b). Grouping of the interval-mean directions was improved after tilt correction. Thus, we conclude that the ChRM direction was likely acquired at, or close to, the time of rock formation.

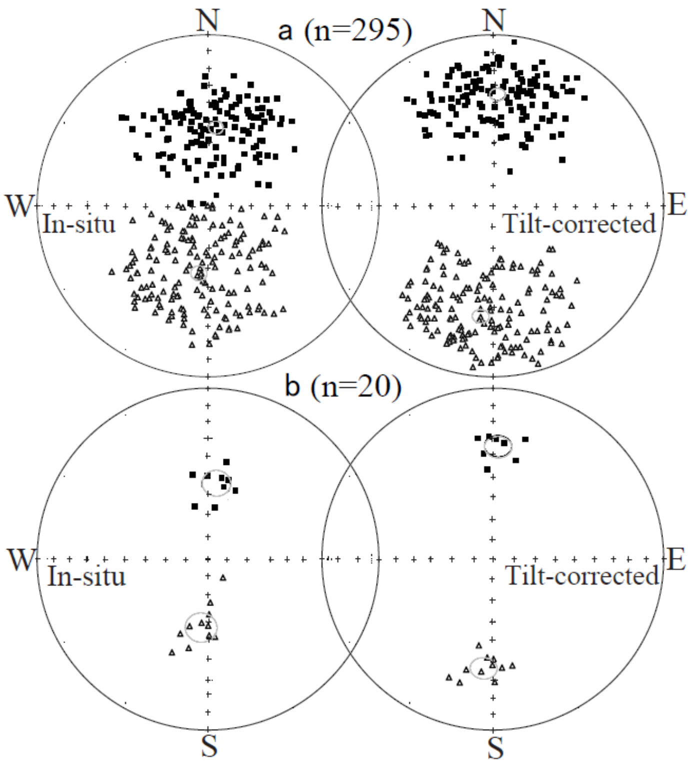

Supp. Figure 3. Maps of equal-area projection (a) 295 ChRM directions and (b) 20 group mean directions of ChRM from the studied Paleocene part of the XJD section before and after tilt correction. All squares (up triangles) represent downward (upward) inclinations.

The ChRM declination and inclination were used to calculate the latitude of virtual geomagnetic pole (VGP). The palaeomagnetic declination and inclination, and VGP latitude from the lower part of the XJD section were used to illustrate the magnetic polarity of the stratigraphic level (Supp. Figure 4). We correlated our magnetic polarity column with the documented Geomagnetic Polarity Time Scale (GPTS) of Ogg (2012) with continuation of the previous paleomagnetostratigraphic work (Jiang et al., 2014).

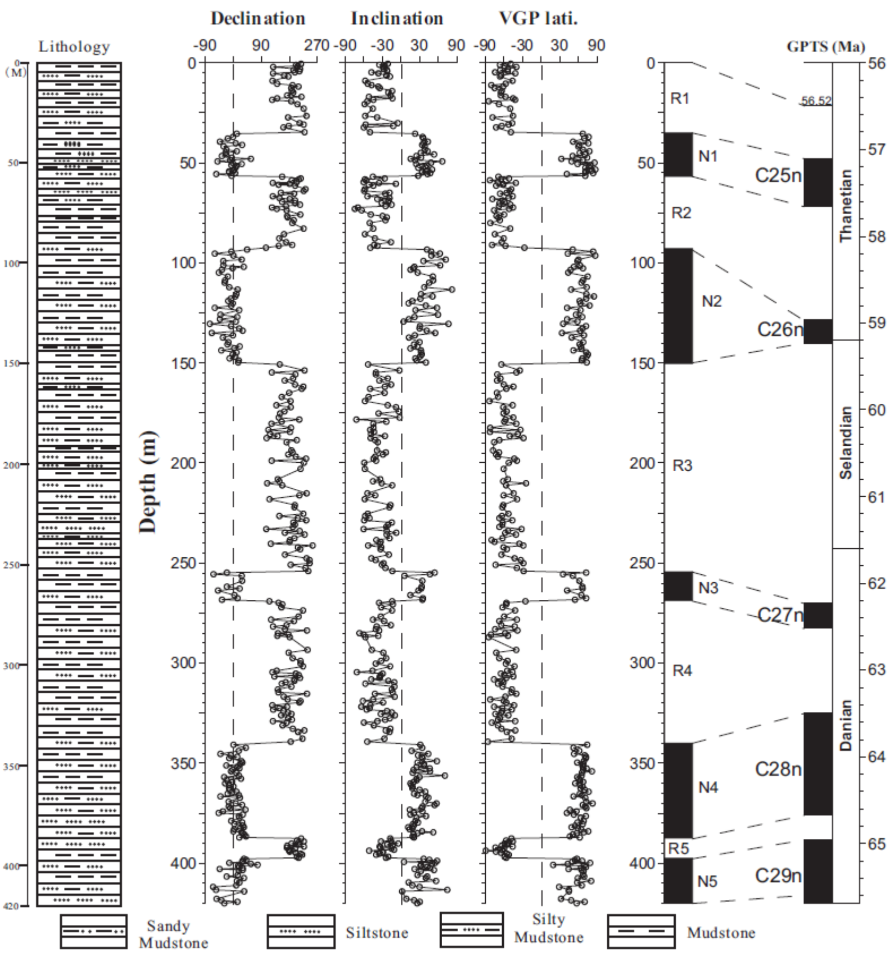

Supp. Figure 4. Lithology and magnetostratigraphy of the Paleocene part of the XJD section and its correlation with the GPTS (Ogg, 2012).

Five normal (N1-N5) and 5 reversed polarity zones (R1-R5) are observed in the lower part of the XJD section (Supp. Figure 4). All normal polarity zones can readily be correlated one by one with C25n-C29n. Given that the strata around N2 from 95 to 150 m is intercalated with several beds of coarse sandstones, the N2 appears much thicker than the correlative C26n so that C26n relative to N2 appears much short in duration (Supp. Figure 4).

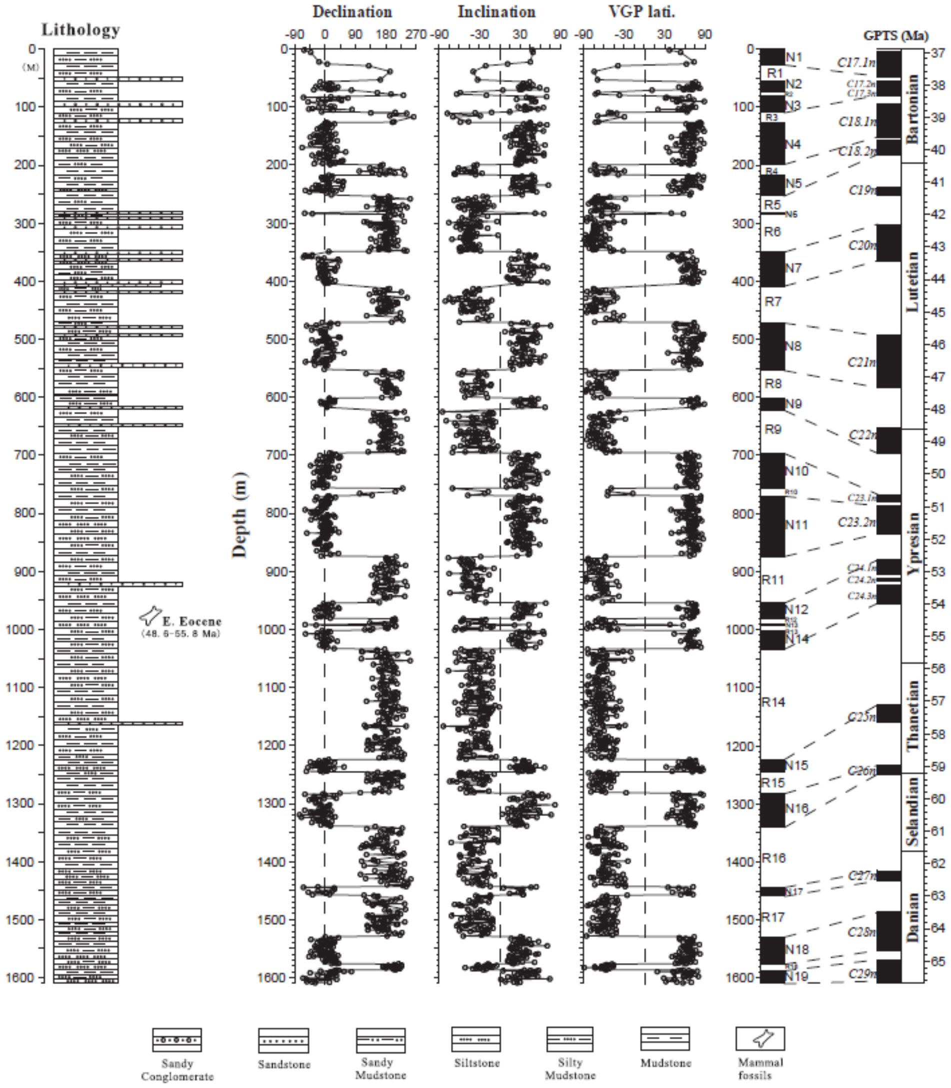

Supp. Figure 5. Lithological column and magnetostratigraphy of the entire XJD section and its correlation with the GPTS (Ogg, 2012). In this study, new magnetostratigraphic work focused on the lower part (420 m) of this section, and that of the upper part was integrated previous work (Jiang et al., 2014).

After integrating with the previous Eocene work (Jiang et al., 2014), the XJD magnetic polarity column shows an unambiguous and reliable correlation with the GPTS of Ogg (2012) (Supp. Figure 5). This correlation suggests that the XJD section is generally continuous, spanning from 65.6 Ma to 37.6 Ma (Supp. Figure 5). Variations of mean sedimentation rate (MSR) with time reveal four short intervals of high MSR (Supp. Figure 6). Beside these four intervals, generally low MSR of the XJD sequence is consistent with the predominance by windblown deposits (Jiang et al., 2014). Based on the magnetostratigraphic result, age control for all the samples is derived from linearly interpolating.

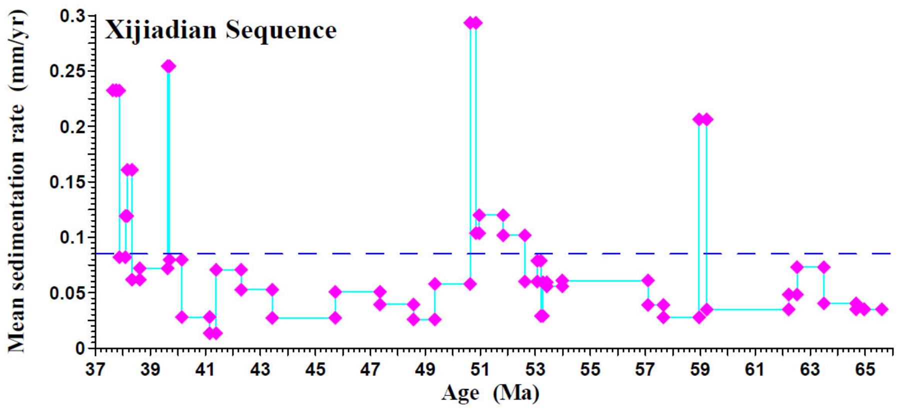

Supp. Figure 6. Age versus mean sedimentation rate of the entire XJD section in the western Nanyang Basin, Hubei Province, East China.

3. Grain-size analysis of the XJD section

Numerical unmixing of grain-size distribution data into constituent components, known as end-member analysis (EMA), can yield valuable information on transport dynamics (Weltje, 1997; Paterson and Heslop, 2015). We analyzed the grain-size data of a total of 5877 samples from the XJD sequence (65.6-37.6 Ma) as a whole. In the correlation maps (Figure 3b & c), R^2 increases from 0.905 to 0.967 and the angle decreases from 14.9° to 8.6° from 2 to 3 end members, but the former increases slightly from 0.967 to 0.984 and the latter only decreases from 8.6° to 5.9° from 3 to 4 end members. This suggests that end-member modeling improves greatly from 2 to 3 end members, but improves fairly less from 3 to 4 end members (Figure 3b & c). For the modeling situations of 4 and 5 end members, the coarsest end-members peak at 127 μm and 175.8 μm, respectively, which are inconsistent with a unimodal distribution mainly concentrated in the range of 0-100 μm (Figure 3a). Their corresponding mean abundances are no more than 10% (8.7% and 4.1%) (Supp. Figure 7). Furthermore, all the other end members are clustered at several to tens microns. Such combination of end members cannot provide reasonable explanation as three end-members, and thus three end-members are the minimum number of end members that are closest to the truth in this study. (Supplementary Note 3)

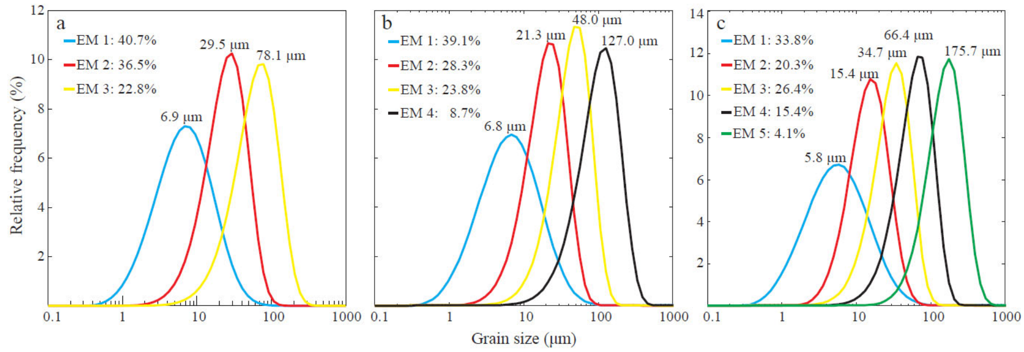

Supp. Figure 7. End-member modeling results of 3-5 end members for all 5877 samples.

Mean grain size (Ms), standard deviation (σ), skewness (Sk), and kurtosis (K_G) are commonly used to discriminate among different depositional processes and environments.

Sahu (1964) distinguished the aeolian process from the littoral environment using the following equation:

$$Y = -3.5688\ Ms + 3.7016\ \sigma^2 - 2.0766\ Sk + 3.1135\ K_G \qquad (1)$$

The Y values for all of the Xijiadian grain-size samples are less than -2.74, indicating an eolian environment (Sahu, 1964). (Supplementary Note 1)

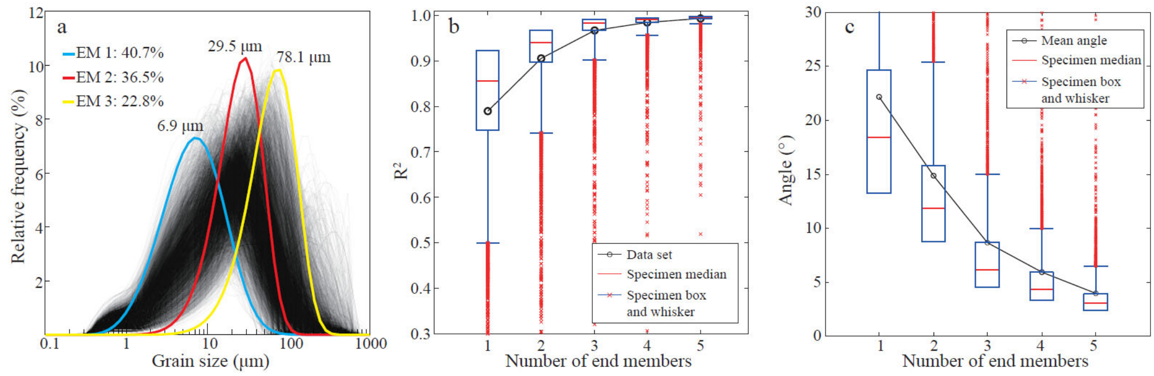

Supp. Figure 8. Grain-size distribution of all 5877 samples and peak values of three end-members (a), linear correlations (R^2) with number of end-members (b) and angular deviation with number of end-members (c). Three end-members have a very high R^2 value of 0.967, implying very good end-member modelling.

4. Major/trace element analysis

According to the newly acquired Paleocene-Eocene chronology frame of the XJD sequence, 136 samples were collected for major/trace element analysis. All the bulk samples for major and trace elemental measurements were ground after air drying and splitting. Each sample was immersed in 40 ml of 1 M acetic acid (HAC) solution at room temperature to remove the carbonates. The residual acid insoluble fractions were washed twice with deionized water and separated by centrifuge, dried at 105°C and ground to 200 mesh in an agate mortar.

Major and trace elemental concentrations of the XJD powder samples were measured on the Philips PW2404 X-ray Fluorescence Spectrometer and the Finnigan MAT HR-ICP-MS (Element I) instrument, respectively, at Analytical Laboratory of Beijing Research Institute of Uranium Geology, China. Powder samples were dried at 40 °C and ground to 200 mesh size (about < 75 μm). Approximately 0.6 g of dry-ground samples were mixed with 5.200 g of $Li_2B_4O_7$ and 0.400 g of LiF in platinum crucibles, heated to 1100 °C for 15 min in a furnace and finally cooled down to form a glass disc for the major element analysis. Analytical uncertainties for the major elements (SiO_2, Al_2O_3, CaO, $Fe_2O_{3(Total)}$, K_2O, TiO_2, MnO, Na_2O and P_2O_5) are less than 3%. Loss on ignition (LOI) was obtained by weighing after combustion 1 h at 1000 °C.

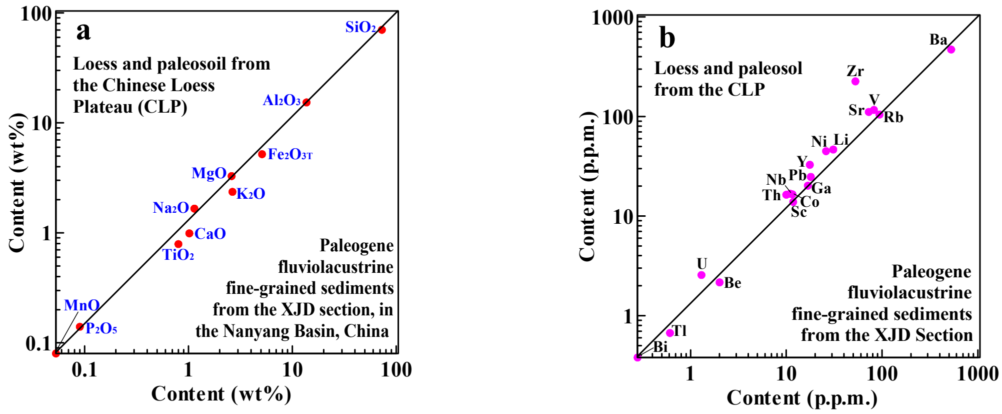

Supp. Figure 9. Comparison of major and trace element compositions between the Paleocene-Eocene lacustrine sediments from the XJD section (average of relatively uniformly distributed 136 samples) and the loess and paleosol from the Chinese Loess Plateau (average of 15 samples) (Ding et al., 2001). (a) Major element compositions and (b) trace element compositions.

The dry-ground samples of 0.05 g for trace element analysis were placed in airtight Teflon vessels. The samples were wetted and shaken lightly to disperse them completely. Five ml of HNO_3 and one ml of HF were added, and vessels were heated on a hot plate (200 °C) for 24 h for dissolution. After the solution was dried, 3-5 ml of HNO_3 was added and the vessels were covered for sufficient dissolution. The solution was sealed and put in an oven with 130 °C for 3 h. The solution was then diluted by 1% HNO_3 and transferred into 50 ml volumetric flasks for elemental measurements. Replicate analyses show good reproducibility and analytical uncertainties less than 10% for most of the trace elements.

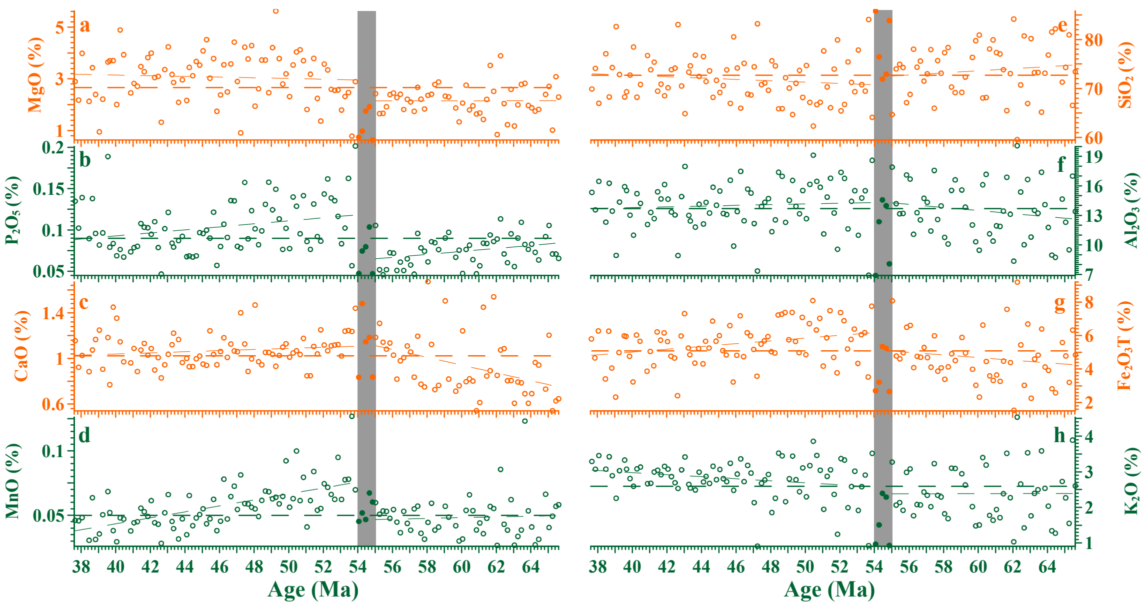

Supp. Figure 10. Major element abundances of the lacustrine samples from the XJD sequence in the Hubei Province, including MgO, P_2O_5, CaO, MnO, SiO_2, Al_2O_3, Fe_2O_{3T} and K_2O. They all show marked changes at 55-54 Ma.

The content of immobile TiO_2 varied from 0.70% to 0.85% with an average of 0.74% in loess and ranged from 0.72% to 0.88% with a mean of 0.80% in paleosol, and its average increased from loess to paleosol mainly due to other mobile elements leaching away (Gallet et al., 1996). In contrast, the mobile Na_2O ranged from 1.42% to 1.76% with a mean of 1.57% in loess and varied from 1.14% to 1.62% with a mean of 1.40% in paleosol in the Chinese Loess Plateau (Gallet et al., 1996). Chemical index of alteration (CIA) is often used as an indicator of the degree of weathering of sediments and is calculated in molecular proportions as follows: CIA = (Al_2O_3/(Al_2O_3+CaO*+Na_2O+K_2O)) × 100 (Nesbitt and Young, 1982), where the CaO* is the amount of CaO in the silicate minerals. (Supp. Note 5)

In this study, the content of immobile TiO_2 had a larger range of fluctuations from 0.46% to 1.21% with a mean of 0.77% (Figure 4a). The content of mobile Na_2O ranged from 0.11% to 3.52% with an average of 1.15% (Figure 4b). In general, TiO_2 had lower values and Na_2O had higher values during 65.6-59 Ma and 55-54 Ma. Moreover, P_2O_5 decreased to below the average from 65.6 Ma to 55 Ma, especially from 59 to 55 Ma, and then jumped to the maximum value at ~54 Ma (Supp. Figure 9b). This sharp increase was probably a response to significant increase in fine-grained particles in the study area, given that P_2O_5 commonly occurs in the smaller size mineral fraction of sediments, such as apatite (Ferrat et al., 2011). After 54 Ma, P_2O_5 gradually decreased although was still above the average on the whole (Supp. Figure 9b).

The CaO concentration in the dust sediments can reflect the variation of calcite content (Ferrat et al., 2011). The abundance of CaO fluctuated most strongly between 65.6 and 59 Ma and then increased from 59 Ma to 55 Ma (Supp. Figure 9c). It oscillated severely at 55-54 Ma and since 54 Ma its generally higher values (0.77%-1.47%, mean 1.07%) varied around the average (1.02%) with small fluctuations. Similarly, abundance of MgO generally fluctuated below the average (2.66%) during 65.6-55 Ma and reached the lowest at 55-54 Ma (0.64-1.92%, mean 1.21%) probably due to dilution by newly added deposits (Supp. Figure 9a). Since 54 Ma, most samples had higher values of MgO than the average with larger oscillating amplitudes, probably in response to an overall strong weathering in the study area. The abundance of MnO was usually below the average (0.05%) during 65.6-55 Ma and increased slightly at 55-54 Ma (Supp. Figure 9d). In addition, SiO_2, Al_2O_3, FeO_T and K_2O all visibly changed at 55-54 Ma (Supp. Figure 9 e-h). (Supplementary Note 4)

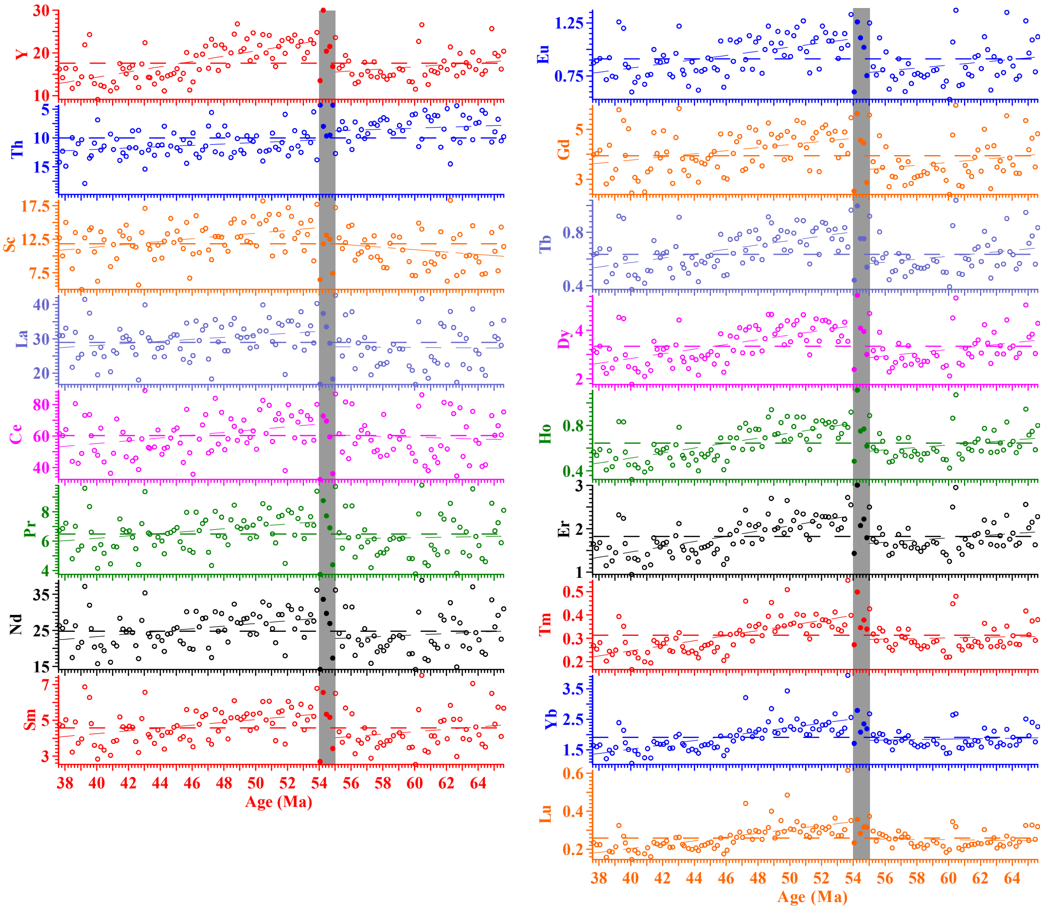

Supp. Figure 11. Marked changes of selected trace element abundances of the lacustrine samples from the XJD sequence in the Hubei Province at 55-54 Ma.

The trace element patterns for terrestrial sedimentary rocks generally reflect the average compositions of the provenance (McLennan, 1989). Some trace elements such as Y, Sc and Th, have been widely applied to provenance studies of atmospheric dust (Jahn et al., 2001; Ferrat et al., 2011; Gallet et al., 1996, 1998; Pease and Tchakerian, 2002; Zdanowicz et al., 2006). In this study, sixteen kinds of trace elements, including Y, Sc, La, Ce, Pr, Nd, Sm, Lu, Yb, Tm, Er, Ho, Dy, Tb, Gd, and Eu, all had a significant increase at 55-54 Ma followed by a gradual decrease since 54 Ma (Supp. Figure 10). Th showed the opposite changes in content.

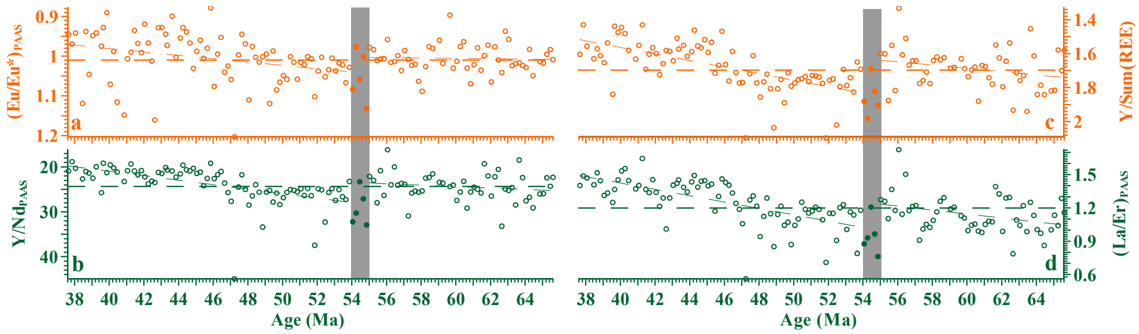

Supp. Figure 12. Selected trace element ratios of $(Eu/Eu^*)_{PAAS}$ (a), Y/Nd_{PAAS} (b), $Y/\Sigma REE$ (c), and $(La/Er)_{PAAS}$ (d) normalized to post-Archean Australian shale (PAAS) for the fluviolacustrine samples from the XJD sequence in the Hubei Province at 55-54 Ma. Changes in these trace elements are independent of particle size. These ratios show marked changes at 55-54 Ma.

5. Clay mineral and Sr-Nd isotope analysis

In this study, a total of 104 samples from the XJD section were collected for measurements of clay mineral composition and 10 samples were chosen for the analysis of Sr–Nd isotope composition of the < 2 μm silicate fraction. These were selected in order to define their potential source areas and weathering history.

Clay mineral analysis of 104 samples and Sr-Nd isotope analysis of 10 samples were carried out on the < 2 μm fraction, which was separated using the Stokes' settling velocity principle, after the removal of carbonate and organic matter. Clay minerals were identified by X-ray diffraction (XRD) using a D8 ADVANCE diffractometer with CuK (alpha) radiation (40 kV, 40 mA) in the Laboratory of the Institute of Oceanology, Chinese Academy of Sciences (IOCAS), based on the routine XRD analysis (Wan et al., 2012). Semi-quantitative estimates of peak areas of the basal reflection for the main clay mineral groups (smectite – 17 Å, illite – 10 Å, palygoskite – 8.3 Å, and kaolinite/chlorite – 7 Å) were carried out on the glycolated samples using the empirical factors of Biscaye (1965). Relative clay mineral abundances are given in percentage. Replicate analysis of the same sample produced results with a relative uncertainty of ± 5%. The illite chemistry index was estimated using the ratio of the peak areas for 5 Å and 10 Å in the ethylene-glycolated samples. Illite crystallinity was calculated as the full width at half maximum height (FWHM) of the illite 10 Å peak. These parameters are usually used to indicate the composition and crystallinity of clay mineral and thus track its source regions and transport paths (Wan et al., 2012).

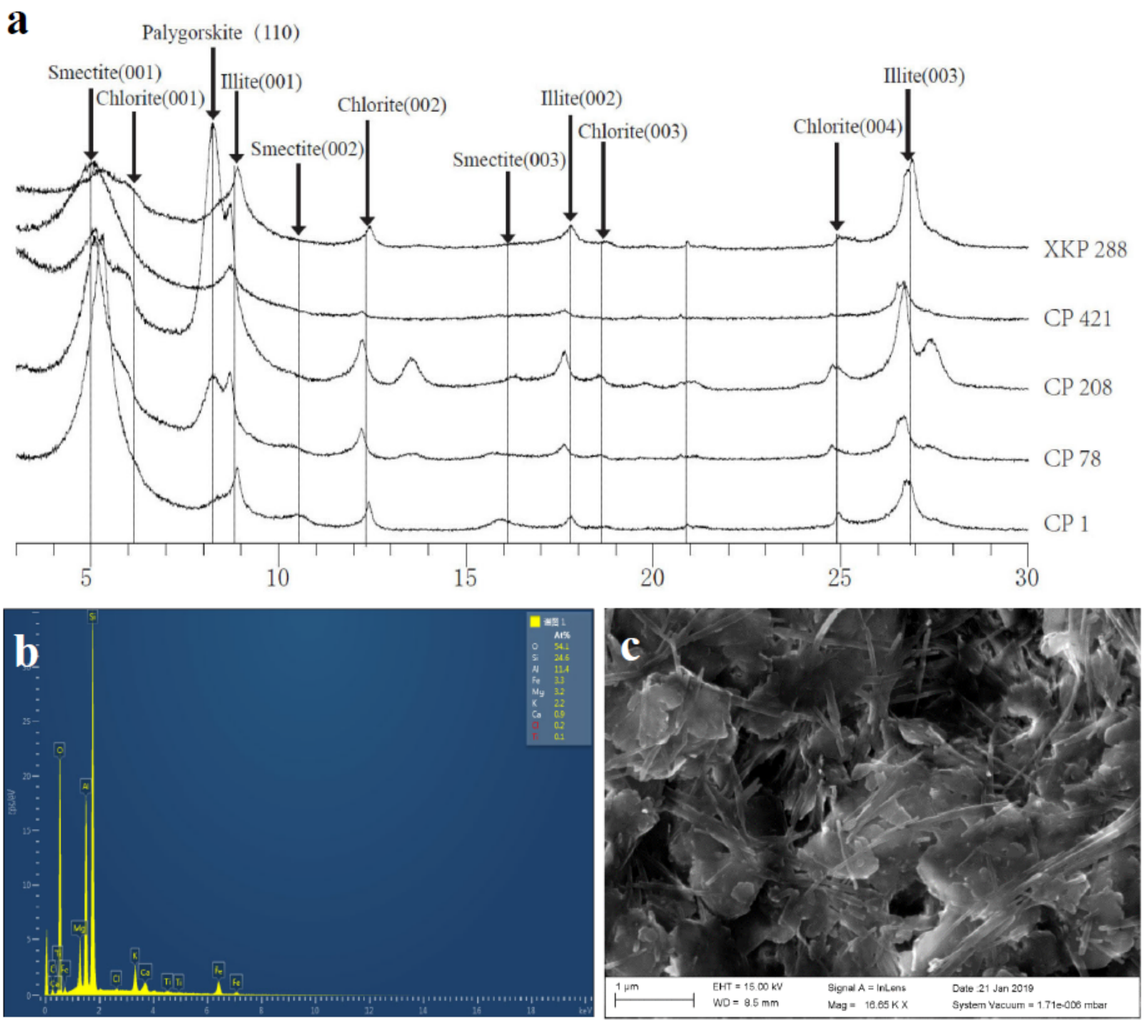

Supp. Figure 13. a. Multiple X-ray diffractograms of typical samples from the XJD sequence. Illite, smectite and palygorskite were major clay minerals. **b**. Characteristic peaks on the energy spectrum of typical samples from the XJD sequence. Five major peaks of Si, O, Al, Mg and Fe have the atomic ratio of 54:24:11:3:3, which is consistent with the feature of palygorskite. **c**. SEM micrograph showing high quantities of locally neoformed palygorskite with development of long palygorskite fibres.

Integrated analyses of X-ray diffratograms, energy spectrum, and fibrous morphology observed under scanning electron microscope (Supp. Figure 12) confirm the presence of palygorskite in nearly all samples. This indicates an overall dry and alkaline depositional environment from 65.6 Ma to 37.6 Ma (Singer, 1984).

The clay mineral assemblages of the XJD sequence were dominated by smectite (6-91%, mean 36%), illite (7-60%, mean 34%) and palygorskite (0-59%, mean 25%), whereas chlorite (0-9%, mean 2%) and kaolinite (0-7%, mean 2%) were less abundant (Figure 4d-f, Supp. Figure 12, Supp. Table 2).

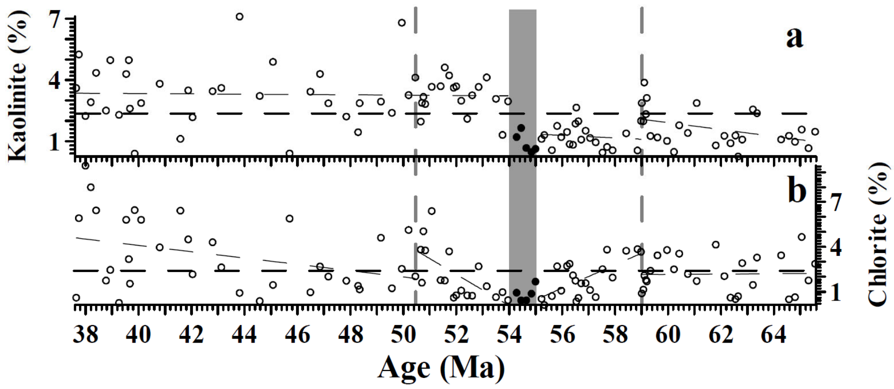

Supp. Figure 14. Abundance distribution of clay minerals kaolinite and chlorite for the Xijiadian sequence spanning 65.6-37.6 Ma plotted against palaeomagnetic ages.

For Sr and Nd isotope analysis, about 200 mg of the < 2 μm fraction were weighed and dissolved in a mixture of ultrapure HNO_3 + HF + $HClO_4$ for 24 h. Sr and Nd fractions were separated using standard ion exchange techniques (Révillon et al., 2011). Sr and Nd isotope compositions were measured in static mode on a Thermo TRITON at the Beijing Institute of Uranium Geology, China National Nuclear Corporation, Beijing, China. All measured Sr and Nd ratios were normalized to $^{86}Sr/^{88}Sr$ = 0.1194 and $^{146}Nd/^{144}Nd$ = 0.7219, respectively. During the analysis, Sr isotope compositions of standard NBS987 gave $^{87}Sr/^{86}Sr$ = 0.710259 ± 7 (n = 9, recommended value 0.710250); Nd standard JNdi-1 gave 0.512102 ± 6 (n = 3, recommended value 0.512100).

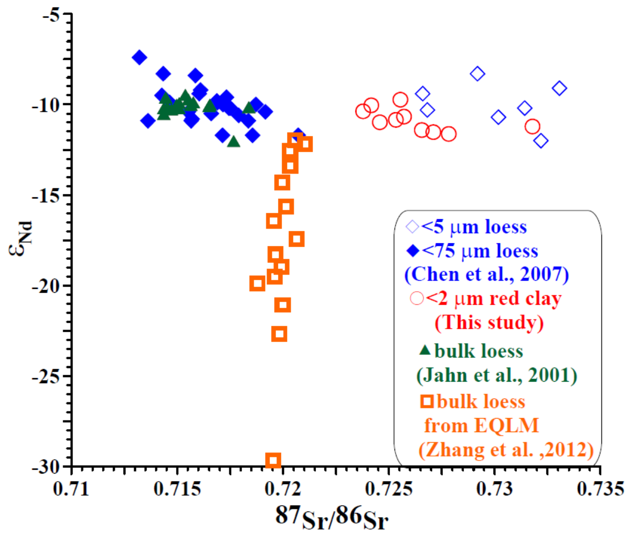

Supp. Figure 15. Sr-Nd isotopic compositions of the fluviolacustrine clay samples from the XJD sequence in the Hubei Province during the Paleocene-Eocene period. Isotopic compositions of the potential sources of Asian dust and the Chinese Loess Plateau (CLP) loess from Chen et al. (2007), Jahn et al. (2001) and Zhang et al. (2012). EQLM means eastern Qinling Mountains.

Nd and Sr isotopes are important tools for fingerprinting Cenozoic clastic sediment sources, especially in the eolian environments (Jahn et al., 2001; Chen et al., 2007; Goldstein et al., 1984). For loess, paleosol and red clay samples from the Lingtai section in the CLP, $^{87}Sr/^{86}Sr$ ratios vary between 0.725733 and 0.729943 with a mean value of 0.727312 for the clay-sized samples and range from 0.720509 to 0.721554 with an average of 0.721005 for the bulk samples. The high $^{87}Sr/^{86}Sr$ ratio is possibly because the clay minerals, especially the K-rich illite, have high content of Rb (Chen et al., 2007). The loess-paleosol sequences of the Xining, Xifeng, and Jixian sections (~800 km apart from Xining to Jixian) in North China show very similar geochemical characteristics, including uniform REE patterns with ~10 of $(La/Yb)_N$, ~0.65 of Eu/Eu*, and ~ -10 of ε_{Nd}, pointing to a distant and homogeneous source region (Jahn et al., 2001). In this study, our samples show uniform REE patterns with ~10.35 of $(La/Yb)_N$, ~0.62 of Eu/Eu*, and ~ -10.8 of ε_{Nd}, which are much similar to those of the eolian or fine-grained deposits from the CLP and desert deposits from the northern margin of the TP (isotope region B, Chen et al., 2007), such as Taklimakan Desert and Qaidam Desert. On the other hand, the loess and paleosol from the eastern Qinling Mountains have a mean $^{87}Sr/^{86}Sr$ ratio of 0.720001 (from 0.718807 to 0.721043) and an average ε_{Nd} of -17.60 (from -29.66 to -11.98), pointing to a proximal clastic contributor apparently derived from the weathered bedrock in the Qinling orogen (Zhang et al., 2012) (Supp. Figure 14). Accordingly, these data suggest that mountainous erosion from the northern margin of the TP probably provided a major fine-grained dust provenance for our study area. (Supplementary Note 2)

Sr and Nd isotopic compositions for the clay fraction (< 2 μm) of the XJD section are relatively uniform with small variations. The $^{87}Sr/^{86}Sr$ ratios varied between 0.723782 and 0.731787 with a mean of 0.726238, and ε_{Nd} ranged from -11.6 to -9.7 with an average of -10.8 (Supp. Table 1 and Supp. Figure 14). Comparison with published isotopic compositions of the potential sources of Asian dust suggests that clay minerals in our study area were primarily derived from the northern margin of the Tibetan Plateau (Jahn et al., 2001; Chen et al., 2007; Zhang et al., 2012). This interpretation is also supported by correlation analysis of main clay mineral content.

A pronounced inverse correlation occurred between the content of smectite and palygorskite (Figure 4d and e, R^2 = -0.756, n = 104, Supp. Figure 15a), suggesting the authigenic transformation of palygorskite from smectite. Furthermore, the abundance of illite (Figure 4f) significantly showed an inverse correlation with the sum of palygorskite and smectite (R^2 = -0.987, n = 104, Supp. Figure 15b). This indicates that illite in the study area was mainly transported by the westerly wind from the northern margin of the TP. This interpretation is further supported by both low chemical index (mean 0.23) and crystallinity (mean 0.40° Δ2θ) of illite (Supp. Table 2), which reflects strong physical erosion and weak chemical weathering.

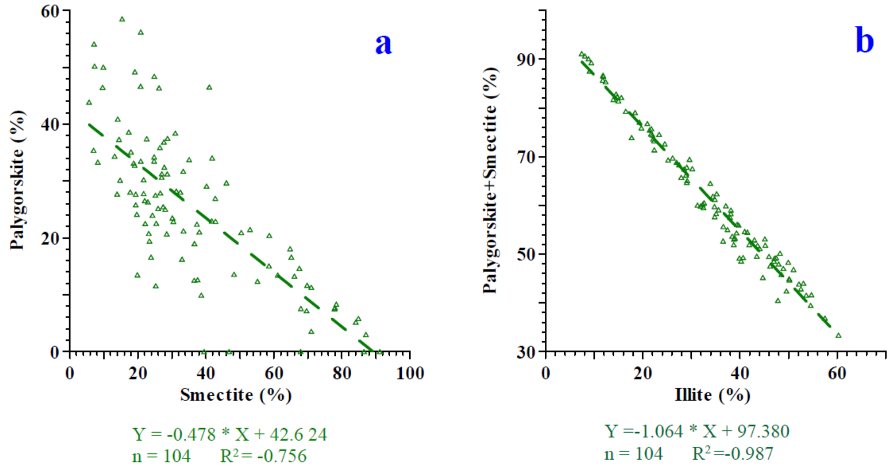

Supp. Figure 16. Correlation maps of the lacustrine clay samples from the XJD sequence in the Hubei Province during the Paleocene-Eocene period. Note that (a) a strong inverse relationship existed between smectite and palygorskite and (b) a stronger one existed between illite and the sum of smectite and palygorskite.

6. Strong tectonic activities in Central to East Asia at 55-54 Ma

We proposed that tectonic activities strengthened at 55-54 Ma based on detailed analysis of grain size, geochemistry and clay minerals of the XJD lacustrine sediments. Besides our study area, previous results (Figure 5) indicated that strong tectonic activity at 55-54 Ma occurred in many regions and resulted in regional disconformities (Kalakot and Salal, Singh, 2003; Erlian Basin, Wang et al., 2010; Zhangshanji, Zheng et al., 1999; Jinhu Depression, Zhou et al., 2019; Taibei Depression, Liu et al., 2020), the onset of India-Eurasia terrestrial faunal exchange (Cambay, Clementz et al., 2011), an abrupt increase in sediment accumulation in the Hoh Xil Basin (Jin et al., 2018), facies transition in the Xigaze forearc Basin (Orme et al., 2015), paleolatitudinal intersection (Ma et al., 2014), thermal remagnetization (Tong et al., 2008), and the new formation of many basins in Asia, such as the Qaidam Basin (Ke et al., 2013), the Xining Basin (Fang et al., 2019), Oytag Basin (Sun and Jiang, 2013), and Lanzhou Basin (Zhang et al., 2014), and even the closing of Neo-Tethys Ocean (Li et al., 2015) (Figure 5, Supp. Table 3). Furthermore, the strong tectonic activity resulted in widespread volcanic activity in Asia, such as Linzhou (54 Ma, Zhou et al., 2004), Mendui (55 Ma, Sun et al., 2010), Aksav (54 Ma, Bazhenov and Mikolaichuk, 2002), Xilutian (~55 Ma, Chen et al., 2014), and Houzhen (~55.7 ± 0.9 Ma, Li et al., 1989) (Figure 5, Supp. Table 3). These datasets indicate that stratigraphy is the best direct way to pinpoint the collision chronology. (Supplementary Note 6)

Newly acquired seismic reflection data confirmed the existence of small fault-controlled basins on the Yandang Low Uplift in the East China Sea Shelf Basin, which presumably formed in the Late Cretaceous and Paleocene (Yang et al., 2019). Faults in and around these basins extend predominantly in NE-NNE and E-W directions and were driven by the westward-dipping boundary faults and the escaping dynamics of the South China Continent because the South China Continent is located at the corner of China continent of the Eurasia plate and suffered the influence from the westward subduction of the western Pacific plate and uplift of the Qinghai-Tibet Plateau (Zhang et al., 2013).

Reference

Biscaye, P.E., 1965. Mineralogy and sedimentation of recent deep-sea clay in the Atlantic Ocean and adjacent seas and oceans. Geol. Soc. Am. Bull.76, 803-832.

Chen, J., Li, G.J., Yang, J.D., Rao, W.B., Lu, H.Y., Balsam, W., Sun, Y.B., Ji, J.F., 2007. Nd and Sr isotopic characteristics of Chinese deserts: Implications for the provenances of Asian dust. Geochimica et Cosmochimica Acta 71, 3904-3914.

Gallet, S., Jahn, B.M. and Torii, M., 1996. Geochemical characterization of the Luochuan loess-paleosol sequence, China, and paleoclimatic implications. Chem. Geol. 133, 67-88.

Gallet, S., Jahn, B.M., Lanoe, B.V., Dia, A., and Rossello, E., 1998. Loess geochemistry and its implications for particle origin and composition of the upper continental crust. Earth Planet. Sci. Lett. 156, 157-172.

Goldstein, S.L., O'Nions, R.K., Hamilton, P.J., 1984. A Sm-Nd isotopic study of atmospheric dusts and particulates from major river systems. Earth Planet. Sci. Lett. 70, 221-236.

Hacker, B.R., Wang, X., Eide, E.A., Ratschbacker, L., 1996. The Qinling-Dabie ultra-high-pressure collisional orogeny. In: Yin, A., Harrison, T.M. (Eds.), The Tectonic Evolution of Asia. Cambridge University Press, Cambrideg, pp. 345-370.

Ke, X., Ji, J.L., Zhang, K.X., Kou, X.H., Song, B.W. and Wang, C.W., 2013. Magnetostratigraphy and anisotropy of magnetic susceptibility of the Lulehe Formation in the northeastern Qaidam Basin. Acta Geologica Sinica 87, 576-587.

Liu, J.S., Xu, H.Z., Jiang, Y.M., Wang, J., He, X.J., 2020. Mesozoic and Cenozoic basin structure and tectonic evolution in the East China Sea basin. Acta Geologica Sinica 94, 675-691.

McFadden, P.L. and McElhinny, M.W., 1990. Classification of the reversal test in palaeomagnetism, Geophys. J. Int., 103, 725-729.

McLennan, S.M., 1989. Rare earth element in sedimentary rocks: influence of provenance and sedimentary process. Reviews in Mineralogy 21, 169-200.

Nesbitt, H.W. and Young, G.M., 1982. Early Proterozoic climates and plate motions inferred from major element chemistry of lutites. Nature 299, 715-717.

Pease, P.P. and Tchakerian, V.P., 2002. Composition and sources of sand in the Wahiba Sand Sea, Sultanate of Oman. Ann. Assoc. Am. Geogr. 92, 416-434.

Révillon, S., Jouet, G., Bayon, G., Rabineau, M., Dennielou, B., Hémond, C., Berné, S., 2011. The provenance of sediments in the Gulf of Lions, western Mediterranean Sea. Geochem. Geophys. Geosyst.12, Q08006, doi:10.1029/2011GC003523.

Singer, A., 1984. The paleoclimatic interpretation of clay minerals in sediments-A review. Earth-Sci. Rev. 21, 251-293.

Wan, S., Yu, Z., Clift, P.D., Sun, H., Li, A., Li, T., 2012. History of Asian eolian input to the West Philippine Sea over the last one million years. Palaeogeogr. Palaeocli-matol. Palaeoecol.326-328, 152-159.

Wang, M. and Shen, Z.-K., 2020. Present-day crustal deformation of continental China derived from GPS and its tectonic implictions. Journal of Geophysical Research: Solid Earth 125, e2019JB018774.

Xu, X.W. and Deng, Q.D., 1996. Nonlinear characteristics of paleoseismicity in China. J.Geophys. Res. 101, 6209-6231.

Yang, C.-S., Yang, C.-Q., Shang, L.-N., Yan, Z.-H., Yang, Y.-Q., 2019. Discovery of Late Cretaceous-Paleocene faulted basins developed on the Yandang Low uplift, East China Sea shelf basin. China Geology 2, 243-244.

Zdanowicz, C., Hall, G., Vaive, J., Amelin, Y., Percival, J., Girard, I., Biscaye, P., and Bory, A., 2006. Asian dustfall in the St. Elias Mountains, Yukon, Canada. Geochim. Cosmochim. Acta 70, 3493-3507.

Zhang, G.W., Guo, A.L., Wang, Y.J., Li, S.Z., Dong, Y.P., Liu, S.F., He, D.F., Cheng, S.Y., Lu, R.K. & Yao, A.P., 2013. Tectonics of South China continent and its implications. Science China Earth Sciences 56, 1804-1828.

Zhang, H.Y., Lu, H.Y., Jiang, S.-Y., Vandenberghe, J., Wang, S.J., Cosgrove, R., 2012. Provenance of loess deposits in the Eastern Qinling Mountains (central China) and their implications for the paleoenvironment. Quaternary Science Reviews 43, 94-102.

Zhang, P.-Z., Gan, W.J., 2008. Combined model of rigid-block motion with continuous deformation: patterns of present-day deformation in continental China. In: Burchfiel, B.C., and Wang, E., eds., Investigations into the Tectonics of the Tibetan Plateau: GSA Spec. Pap. 444, 59-71.